5. THE ARCTIC—M. O. Jeffries and J. Richter-Menge, Eds.

a. Overview—M. O. Jeffries and J. Richter-Menge

The Arctic chapter describes a range of observations of Essential Climate Variables (ECV; Bojinski et al. 2014), and other physical environmental variables. They encompass the atmosphere, ocean, and land in the Arctic and the subarctic.

As in previous years, the 2014 report illustrates that, although there are regional and seasonal variations in the state of the Arctic environmental system, it continues to respond to long-term upward trends in air temperature. Over Arctic lands, the rate of warming is more than twice that of the lower latitudes.

In early 2014 there was a strong connection between the Arctic atmosphere and midlatitude weather due to large north–south excursions of the polar vortex. In Alaska this led to statewide temperature anomalies of +10°C in January, due to warm air advection from the south, while temperature anomalies in eastern North America and Russia were −5°C, due to cold air advection from the north [see sections 7b(2) and 7g(2) for more details].

The mean annual Arctic land surface air temperature anomaly for 2014 (+1.1°C relative to the 1981–2010 average) was the fourth warmest in the record (1900–present) and continued a pattern of increasing positive anomalies since the late 20th century. Warming and its effect on other components of the Arctic environment were exemplified in spring 2014 by a strong positive air temperature anomaly in Eurasia of as much as +4°C relative to the 1981–2010 average. Consequently, snow cover extent in April 2014 was the lowest since satellite observations began in 1967, and snow melt occurred 20–30 days earlier than the 1998–2010 average. In western Eurasia and Scandinavia, spring break-up of lake ice was 21–42 days earlier than the 2004–13 average. In contrast, lake ice break-up in eastern Siberia and the Canadian Arctic Archipelago was 7–21 days later than average.

Evidence is emerging that Arctic warming is driving synchronous pan-Arctic responses in the terrestrial and marine cryosphere that are strengthening over time. For instance, for the period of satellite observation (1979–2014) the rate of summer sea ice loss (−13.3% decade^{-1} decline in minimum ice extent) falls squarely between the rates of Northern Hemisphere snow loss in May and June (−7.3% and −19.8% decade^{-1}, respectively, decline in snow cover extent). In September 2014, minimum sea ice extent was the sixth lowest since satellite records began in 1979. The eight lowest sea ice extents during this period have all occurred in the last eight years (2007–14).

As the sea ice retreats in summer, sea surface temperature (SST) in all the marginal seas of the Arctic Ocean is increasing. The most significant linear trend is in the Chukchi Sea, where SST increased at a rate of 0.5°C decade^{-1} over the period 1982–2010. In summer 2014, the largest SST anomalies (as much as 4°C above the 1982–2010 average) occurred in the Barents Sea and in the Bering Strait–Chukchi Sea region.

Immediately east of the Chukchi Sea, on the North Slope of Alaska, new record high temperatures at 20-m depth were measured at four of the five permafrost observatories. Permafrost temperature at 20-m depth on the North Slope has increased between 0.18° and 0.56°C decade^{-1} since 2000. Permafrost warming in northernmost Alaska exemplifies what is happening to permafrost temperature on a pan-Arctic scale.

Also on land, glaciers and ice caps in Arctic Canada, Alaska, northern Scandinavia and Svalbard, Iceland, and the Greenland Ice Sheet itself, continue to lose mass. The Greenland Ice Sheet also experienced extensive melting again in summer 2014. The maximum extent of melting at the ice sheet surface was 39.3% of its total area and the extent of melting was above the 1981–2010 average for 90% of the time. Average albedo (reflectivity) during summer 2014 was the second lowest since observations began in 2000, with a new, ice sheet-wide record low albedo for the month of August.

At Summit, near the center of the Greenland Ice Sheet, UV radiation in 2014 was strongly anticorrelated with the atmospheric total ozone column (TOC) because it is largely unaffected by cloud variability at this location. Elsewhere in the Arctic, cloud variability was the major influence on UV radiation in 2014. At the pan-Arctic scale, the minimum TOC that occurred in March 2014 was 344 Dobson units, 13% below the 1979–88 average.

The preceding refers to a number of different periods of observation for which average values (also known as normals) and departures from average (anomalies) have been calculated. For many national agencies such as NOAA and the National Snow and Ice Data Center (NSIDC), 1981–2010 is the current reference period for calculating averages and anomalies. In this chapter, 1981–2010 is used whenever possible, but cannot be used for all the variables described because some organizations use different reference periods and because many observational records begin after 1981. The use of different periods to describe the state of different elements of the Arctic environmental system is unavoidable, but it does not alter the fact that change is occurring throughout the Arctic environmental system in response to increasing air temperatures.

b. Air temperature—J. Overland, E. Hanna, I. Hanssen-Bauer, S.-J. Kim, J. Walsh, M. Wang, and U. S. Bhatt

Arctic air temperatures are both an indicator and driver of regional and global changes. The mean annual surface air temperature anomaly of +1.1°C (relative to the 1981–2010 mean value) for 2014 for land stations north of 60°N continues the pattern of increasing positive anomalies since the late 20th century (Fig. 5.1). Over land surfaces, based on the CRUTEM4 dataset, 2014 was the fourth warmest year in the Arctic record and globally the fifth warmest, with most of the warmest years on record occurring since 2000.

The global rate of air temperature increase has slowed in the last decade (Kosaka and Xie 2013), but Arctic temperatures have continued to increase at a fairly constant rate since 1980 (Fig. 5.1). The Arctic is now warming at more than twice the rate of lower latitudes (Overland et al. 2014a). The rapid warming in the Arctic is known as Arctic amplification and is due to feedbacks involving many parts of the Arctic environment: loss of sea ice and snow cover, changes in land ice and vegetation cover, and atmospheric water vapor content (Serreze and Barry 2011). There are year-to-year and regional differences in air temperatures due to natural chaotic variability, but the magnitude and Arctic-wide character of the long-term temperature increase, and particularly the early 21st century increase, is a major indicator of global warming rather than natural regional variability (Overland 2009; Jeffries et al. 2013).

Seasonal air temperature variations are described in Fig. 5.2 for (a) winter (January–March), (b) spring (April–June), (c) summer (July–September), and (d) fall 2014 (October–December). For winter 2014, each month had similar regional temperature extremes (Fig. 5.2a). Extreme monthly positive temperature anomalies in excess of +5°C over the central Arctic

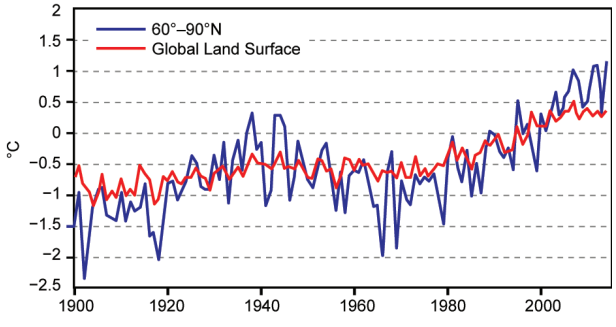

Fig. 5.1. Arctic and global mean annual surface air temperature anomalies (°C) for the period 1900–2014 relative to the 1981–2010 mean value. The data are for land stations only. Results are based on the CRUTEM4v dataset.

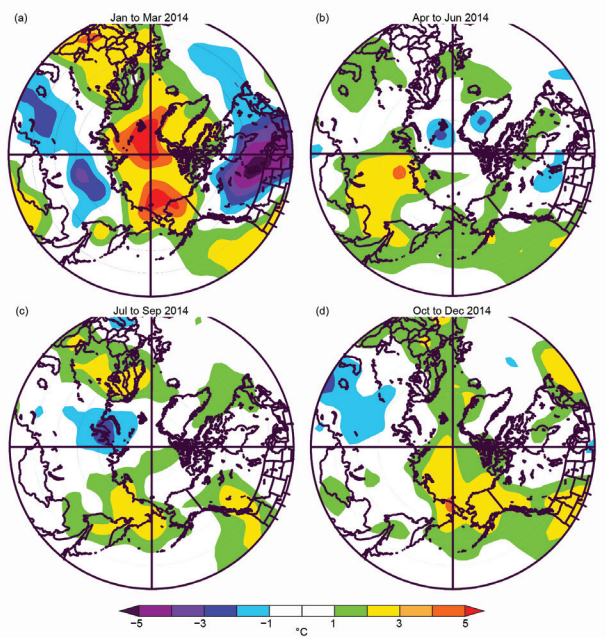

Fig. 5.2. Seasonal anomaly patterns (relative to the baseline period 1981–2010) for near-surface air temperatures (°C) in (a) winter, (b) spring, (c) summer, and (d) fall 2014. Temperature analyses are from slightly above the surface layer (at 925-mb level) to emphasizes large spatial patterns rather than local features. Data are from NCEP/NCAR Reanalysis.

spread south over Europe and Alaska. Svalbard Airport, for example, was 8°C above the 1981–2010 January–March average. In Alaska, statewide temperature anomalies were +10°C in late January. Warm temperatures broke the 7-year (2007–13) sequence of cold anomalies and extensive sea ice cover in the Bering Sea. Conversely, temperature anomalies were 5°C below normal in January and February over eastern North America and in January, February, and March over much of Russia. Northern Siberia was relatively cool, while warm anomalies were observed in far eastern Asia. This pattern resulted from fewer storms connecting central Asia to northern Europe and was perhaps related to the greater-than-average sea ice loss that occurred in winter 2014 over the Barents and Kara Seas (Kim et al. 2014).

On a number of occasions in winter, Arctic and midlatitude weather patterns were strongly linked due to a high amplitude (more sinuous) "wave number 2" jet stream pattern (two high and low pressure regions around a latitude circle), which is illustrated by the seasonal analysis, (Fig. 5.3). This pattern sent warm air from the south northward into Alaska and northern Europe and cold air from the Arctic southward into eastern North America, as evidenced by the higher geopotential heights north of Alaska and central Greenland (Fig. 5.3). A number of recent publications

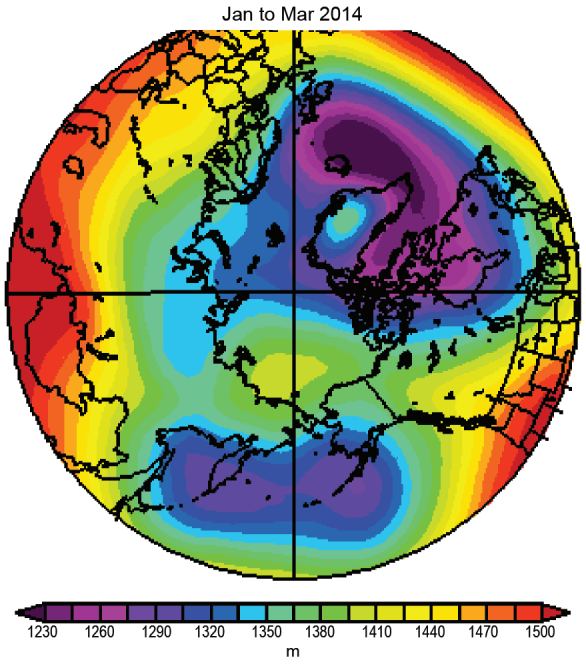

Fig. 5.3. Geopotential height at 850-hPa field (in dynamic meters) for winter Jan–Mar 2014. Wind flow is counter-clockwise along the geopotential height contours. Data are from NCEP/NCAR Reanalysis.

describe the current thinking on the connection between Arctic and midlatitude weather patterns (Cohen et al. 2014; Francis et al. 2014; Vihma, 2014; Barnes and Screen 2015; Francis and Vavrus 2015; Handorf et al. 2015). The wave number 2 pattern had low heights over Iceland, where record-low sea level pressures and warm temperatures occurred. The wave number 2 pattern over eastern North America and the positive North Atlantic Oscillation (NAO) over the North Atlantic Ocean contributed to January flooding in the UK due to more southerly storm tracks and exceptional winter precipitation (Slingo et al. 2014).

In spring, low pressure over the Kara Sea caused warmer temperatures in central Siberia and a record-low April snow cover extent in Eurasia (see section 5d) and localized cold anomalies over Svalbard and at high elevation on the Greenland Ice Sheet (Fig. 5.2b). The Bering Sea region had warm spring air temperature anomalies, unlike the cold temperature anomalies of the previous six years.

Air temperatures were near-normal during summer 2014 over the central Arctic basin (Fig. 5.2c) relative to the 1981–2010 average, which includes a number of warm years. A low pressure region in the summer over north central Siberia (Fig. 5.4) caused a cold temperature anomaly over land to the south of the Kara Sea (due to cold air advection from the Arctic Ocean) and a warm anomaly in northeastern Siberia (due to warm air advection from the continent to the south; Fig. 5.2c). This low pressure region is part of the Arctic dipole, characterized by higher pressure on the North American side of the Arctic than on the Eurasian side (Fig. 5.4), and has been a common summer weather feature in the last decade, when it played a role in the degree of sea ice loss and minimum ice extent (Overland et al. 2012; Wang et al. 2009).

A number of Greenland weather stations reported anomalously high air temperatures in summer 2014 (Tedesco et al. 2014; section 5f). On the opposite side of the North Atlantic Ocean, many weather stations in Scandinavia observed their highest summer air temperatures on record [see section 7f(3) for more details].

In fall, a warm air temperature anomaly extended across the Arctic Ocean from the North Pacific Ocean to the North Atlantic Ocean (Fig. 5.2d). The warm anomaly was particularly pronounced in October over the East Siberian Sea; this has been a recurring feature in recent years when sea ice extent was very low the previous summer compared to the long-term average. November and December air temperatures were associated with a stronger-than-average Aleutian low and Icelandic low. Warm air advection northeastward of these lows contributed to +7°C temperature anomalies in November in Alaska and to warm weather in western Europe. The particularly strong Icelandic low was associated with positive NAO values in November (+0.7) and December (+1.9).

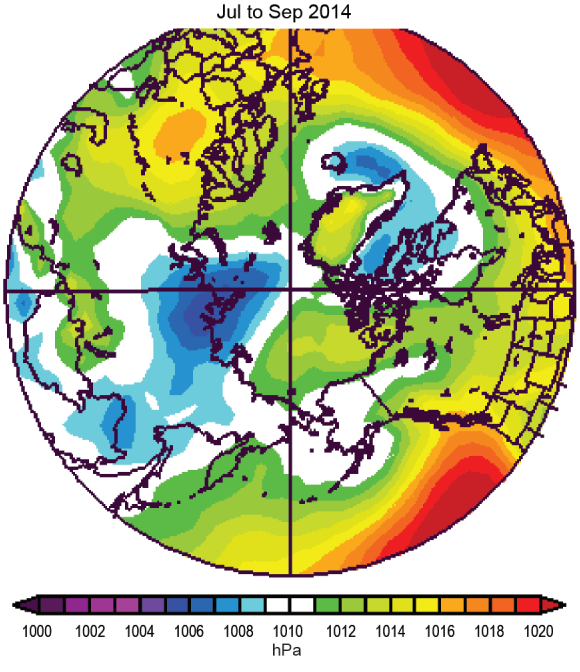

Fig. 5.4. Sea level pressure field (in hPa) for Jul–2014 illustrates the Arctic dipole pattern, with higher pressure on the North American side of the Arctic than on the Eurasian side. Data are from NCEP/NCAR Reanalysis.

SIDEBAR 5.1: CHALLENGE OF ARCTIC CLOUDS AND THEIR IMPLICATIONS FOR SURFACE RADIATION—M. D. SHUPE, M. TJERNSTRÖM, AND P. O. G. PERSSON

Clouds simultaneously serve as a major modulator of the Arctic surface energy budget and as one of the greatest impediments to accurately representing the Arctic system in numerical models. This paradox casts clouds, and their implications, as a grand challenge for Arctic climate science. This challenge is especially salient in a changing Arctic, where influential cloud feedbacks play variable roles and the fate of the cryosphere hangs in the balance. To understand the state and evolution of Arctic climate requires unraveling the emerging story of Arctic clouds and their impacts on radiative budgets.

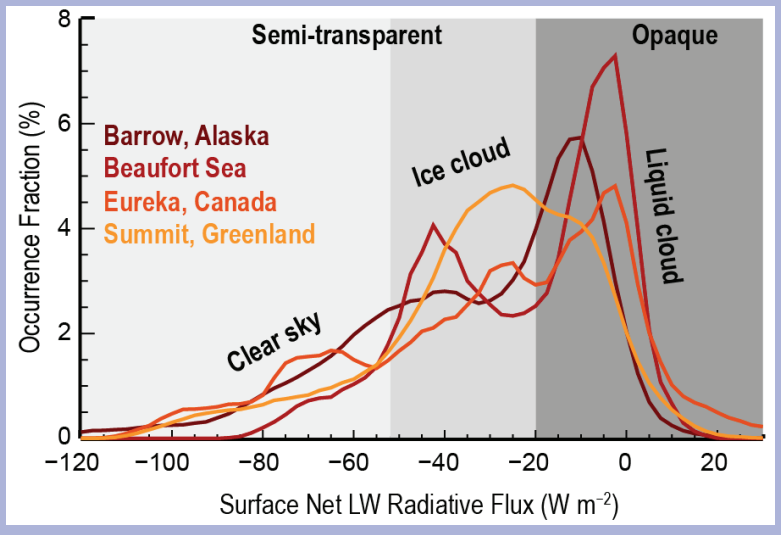

FIG. SB5.1. Distributions of observed net longwave radiation at the surface under clear skies, ice clouds, and liquid clouds at four Arctic locations.

At the surface, clouds have competing radiative influences. They reflect incident solar radiation, serving to cool the surface, while absorbing and re-emitting terrestrial radiation, which warms the surface. For the most part, warming effects dominate throughout the year. The long solar night means that little solar radiation is available to warm the surface, and that surface is largely covered in highly reflective snow and ice. Cooling effects can dominate for a short period in summer, when the sun is highest in the sky and surface reflectance decreases due to melting snow and ice (Curry et al. 1996). Cloud radiative properties are driven, to first order, by the presence and, importantly, phase of clouds. Clouds containing liquid water tend to have a stronger impact on atmospheric radiation (e.g., Shupe and Intrieri 2004). In spite of its tendency to freeze at cold temperatures, cloud liquid water still occurs 10–80% of the time across the Arctic, depending on season and location (Shupe 2011; Cesana et al. 2012).

A growing understanding of Arctic surface longwave radiation related to clouds reveals a two-state system (e.g., Stramler et al. 2011; Fig. SB5.1). One state entails an opaque atmosphere with liquid-containing clouds in near-radiative equilibrium with the surface, while the other state is radiatively clear or semi-transparent and allows the surface to efficiently cool by emitting longwave radiation to space. This second state includes conditions ranging from clear sky to thin clouds that primarily contain ice. Under the opaque state the net longwave radiation is 20–90 W m^{-2} greater than the semi-transparent or clear state (Fig. SB5.1). While other surface energy flux terms often respond to reduce the impact of this radiative forcing, the remaining energy excess at the surface can have important implications for cryospheric change via modified surface temperatures and enhanced melt (e.g., Persson 2012).

Numerical models struggle to represent Arctic surface energy fluxes (Tjernström et al. 2008) in large part due to difficulties in producing the correct cloud types (de Boer et al. 2012). The first-order obstacle is correctly creating and sustaining the supercooled cloud liquid water that contributes to the opaque atmospheric state (Cesana et al. 2012; Pithan et al. 2014). While cloud ice grows at the expense of liquid water at below-freezing temperatures, liquid often persists over long periods via a complex web of local and large-scale processes that can buffer clouds from collapse (Morrison et al. 2012). Key processes involve mixed-phase transitions; cloud particle nucleation; the interplay of microphysics, radiation, dynamics, and turbulence; sensitivity to atmospheric aerosols; and the variable balance of local versus long-range sources of moisture and aerosols. With cloud systems sensitive to so many processes that can manifest on multiple scales, it is not surprising that models do not accurately represent this key component of the Arctic system.

Adding to the challenge is the response of cloud properties, such as occurrence frequency, longevity, and phase partitioning, to broader Arctic changes. Arctic change manifests at the surface via transformations in

the cryosphere (e.g., sea ice thinning and loss), and within the atmosphere via warming, moistening, and modified large-scale dynamics (Graverson et al. 2008). The seasonal response of clouds to change can have significant and varied implications. For example, increases in cloudiness or liquid water occurrence in spring or fall would contribute to enhanced warming, accelerate cryospheric melting, and possibly lengthen melt seasons (Stone et al. 2002; Markus et al. 2009; Persson 2012). On the other hand, increased cloudiness in summer, especially over open water and land areas, would produce a surface cooling effect and slow melt processes. Arctic cloudiness may be increasing in fall and spring, but possibly not in summer (Wang and Key 2003; Kay and Gettelman 2009; Palm et al. 2010), implying that current cloud changes may be amplifying the declines in sea ice, permafrost, and land ice.

Understanding both large-scale and detailed cloud-scale processes, and clarifying the emerging feedbacks between clouds and the evolving Arctic climate system, are key research objectives for the coming decades. Observations over the sea ice pack and open water areas of the Arctic Ocean will be particularly vital for achieving these objectives. Observational and modeling opportunities to address the Arctic cloud and surface radiation challenge include the Multidisciplinary drifting Observatory for the Study of Arctic Climate (MOSAiC) and the Year of Polar Prediction (YOPP, mid-2017 to mid-2019) of the WMO Polar Prediction Project. MOSAiC aims to observe and characterize coupled atmosphere–ice–ocean–ecosystem processes, including cloud processes and the surface energy budget, at a year-long drifting station on the central Arctic sea ice (www.mosaicobservatory.org). The intensive, process-level observations, along with other enhanced measurements across the Arctic, will serve as a key testbed for coupled-system model development and improving predictive capabilities on a range of time scales during the YOPP.

c. Ozone and UV radiation—G. Bernhard, G. Manney, J.-U. Grooß, R. Müller, K. Lakkala, V. Fioletov, T. Koskela, A. Heikkilä, and B. Johnsen

The minimum Arctic daily total ozone column (TOC, the total amount of ozone in a column from Earth's surface to the top of the atmosphere) measured by satellites in March 2014 was 344 Dobson Units (DU). This value was 53 DU (13%) below the average of 397 DU for the period of 1979–88 and 26 DU (7%) below the average for the past decade, 2004–13 (Fig 5.5). The record low was 308 DU in 2011. Figure 5.5 also indicates that the Arctic ozone interannual variability is large: the standard deviation for the period 1979–2014 is 36 DU. This large variability is caused by dynamical effects that affect vortex size and longevity, transport of ozone into the lower stratosphere, and stratospheric chemistry via its sensitivity to temperature (e.g., Tegtmeier et al. 2008; WMO 2014).

Figure 5.6 shows the temporal evolution of ozone concentrations measured between 1 December 2013 and 1 April 2014 at approximately 20-km altitude. These measurements are compared with similar data from winter 2010/11 and the mean and range of values observed between winter 2004/05 and winter 2012/13, excluding the 2010/11 winter. That winter had record low ozone due to unusual meteorological conditions that resulted in a very cold, long-lived vortex with unprecedented chemical ozone loss (e.g., Manney et al. 2011) and weaker-than-usual ozone transport (e.g., Isaksen et al. 2012; Strahan

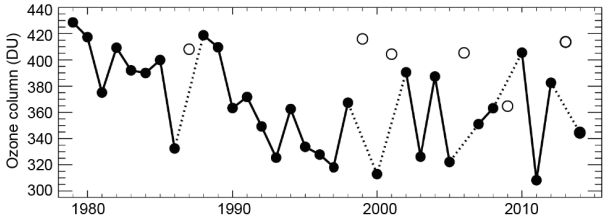

Fig. 5.5. Time series of area-averaged minimum total ozone for March in the Arctic, calculated as the minimum of daily average column ozone poleward of 63° equivalent latitude (Butchart and Remsberg 1986). Open circles represent years in which the polar vortex broke up before March. Ozone in those years was relatively high because of mixing with air from lower latitudes and higher altitudes and a lack of significant chemical ozone depletion. Data are adapted from Müller et al. (2008) and WMO (2014), updated using ERA-Interim reanalysis data (Dee et al. 2011a). Ozone data from 1979–2012 are based on the combined total column ozone database version 2.8 produced by Bodeker Scientific (www.bodekerscientific.com/data/total-column-ozone). Data for 2013 and 2014 are from the Ozone Monitoring Instrument aboard the NASA *Aura* satellite.

et al. 2013). Ozone concentrations at 20 km were chosen because chemical losses at this altitude are large and are representative of loss processes occurring between about 15 km and 25 km. Ozone concentrations in 2014 were above the 2004–13 mean up to early February and below the mean from early March onward. Below-average stratospheric temperatures, which promote chemical ozone loss, were also observed lasting from December through mid-March. The ozone loss in 2014 was much smaller than that in the winter of 2010/11 when low temperatures persisted into April (e.g., Manney et al. 2011). However, because of large interannual variability in the timing and the strength of ozone transport to the Arctic, chemical ozone loss cannot be measured by the temporal evolution of ozone alone. While the chemical ozone loss in 2014 appears to be greater than the 2004–13 mean (excluding 2011), this cannot be assessed with certainty unless ozone changes due to transport are also quantified.

Deviations of monthly average TOCs from historical (1979–88) means were estimated with maps provided by Environment Canada (Fig. 5.7). Monthly average TOCs typically vary by less than ±15% about historical means, but there were several regions in 2014 where anomalies exceeded 15%. In February 2014, three areas with monthly average TOCs more than 15% below the historical mean were roughly centered at the North Pole, northwest Russia, and the Davis Strait. In March, a large area with average TOCs about 15–27% below the mean was centered at the Gydan Peninsula and extended west to east from Norway to the Central Siberian Plateau. In April, the region of low ozone occurred somewhat farther to the east and decreased in area. Between May and November, no areas with monthly ozone anomalies exceeding 15% were observed.

UV radiation is described according to the UV index (UVI), a measure of the ability of UV radiation to cause erythema (sunburn) in human skin (WHO 2002). In addition to its dependence on TOC (see above), the UVI depends greatly on the sun angle, cloud cover, and other factors (Weatherhead et al. 2005). In the Arctic, the UVI scale ranges from 0 to about 7, with sites closest to the North Pole having the smallest peak radiation and UVI values <4 all year. UVI values <5 indicate low to moderate risk of erythema (WHO 2002).

At high latitudes, satellite-based estimates of the surface UVI are subject to large uncertainties (Tanskanen et al. 2007). UV radiation is therefore assessed with ground-based instruments deployed at latitudes between 61° and 73°N in Alaska, Greenland, and Finland (Fig. 5.8). UVI measurements in 2014 are compared with historical measurements. Reference

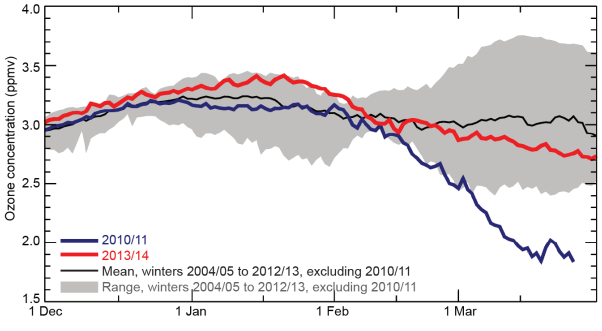

Fig. 5.6. Ozone concentrations measured by the Microwave Limb Sounder (MLS) at the 490 K potential temperature surface (~20 km altitude). Data were averaged over the area of the polar vortex (the band of strong westerly winds in the stratosphere encircling the Arctic in winter). Observations during winter 2013/14 (red line) are compared with similar data from winter 2010/11 (blue line). The black line and gray shading indicate the mean and range, respectively, of values observed between winter 2004/05 and winter 2012/13, excluding the 2010/11 winter. This reference period was chosen based on the availability of MLS data.

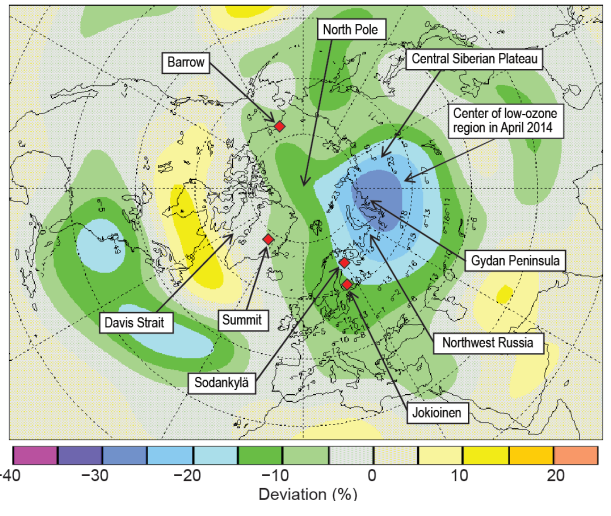

Fig. 5.7. Deviation (in %) of the Dec 2013–March 2014 monthly average TOC from 1979–88 means. The 2014 data are based on ground-based measurements and Ozone Monitoring Instrument (OMI) and Global Ozone Monitoring Experiment–2 satellite data. Reference data are for the period 1979–88 and were calculated by Environment Canada from Total Ozone Mapping Spectrometer (TOMS) observations. Similar maps are available for all months and were used for the assessment of ozone anomalies discussed in the text (http://es-ee.tor.ec.gc.ca/cgi-bin/selectMap). Red diamonds indicate the location of UV spectroradiometers for which data are shown in Fig. 5.8.

periods for each site are different and are based on the available data records.

At Summit, a station located at the center of the Greenland Ice Sheet (Fig. 5.8a), the noon UVI in 2014 was enhanced by up to 33% in February and the beginning of March compared to the 2004–13 mean. In contrast, the UVI was suppressed by up to 29% in mid-March and by up to 28% in September. These anomalies exceeded the range of the 2004–13 reference period for this site. A comparison of the center and bottom panels of Fig. 5.8a indicates that these UVI anomalies tend to be negative when TOC anomalies are positive and vice versa. Clouds over the Greenland ice sheet tend to be optically thin and multiple reflections between clouds and the highly reflective snow surface reduce cloud attenuation further (Nichol et al. 2003). The effect of clouds at Summit is therefore minimal (Bernhard et al. 2008) and UVI variations from TOC changes are only slightly masked by cloud variability

At Barrow, a coastal city located close to the northernmost point of Alaska (Fig. 5.8b), UVI measurements during two periods in February and March 2014 were enhanced by up to 20% above the long-term (1991–2013) mean. The variability of UVI observations between April and November 2014 was mostly within the historical range. The large UVI variability at Barrow between June and October compared to February through May is predominantly caused by cloud effects.

UVI measurements in Scandinavia, represented here by Sodankylä (a site in northern Finland surrounded by boreal forest and peatland; Fig. 5.8c) and Jokioinen (representative of the boreal forest belt of southern Scandinavia; Fig. 5.8d) remained largely within the range of historical records. UVI measurements at the two sites were also mostly controlled by cloud variability.

While data from the few ground stations discussed here cannot provide a comprehensive assessment of UV radiation levels occurring in the Arctic, the relatively modest departure of the TOC from the long-term mean in 2014 suggests that large spikes in UV radiation did not happen during this year.

d. Terrestrial snow cover—C. Derksen, R. Brown, L. Mudryk, and K. Luojus

The Arctic (defined here as land areas north of 60°N) is always completely snow covered in winter, so the transition seasons of fall and spring are of interest when characterizing variability and change. The timing of spring snow melt is particularly significant

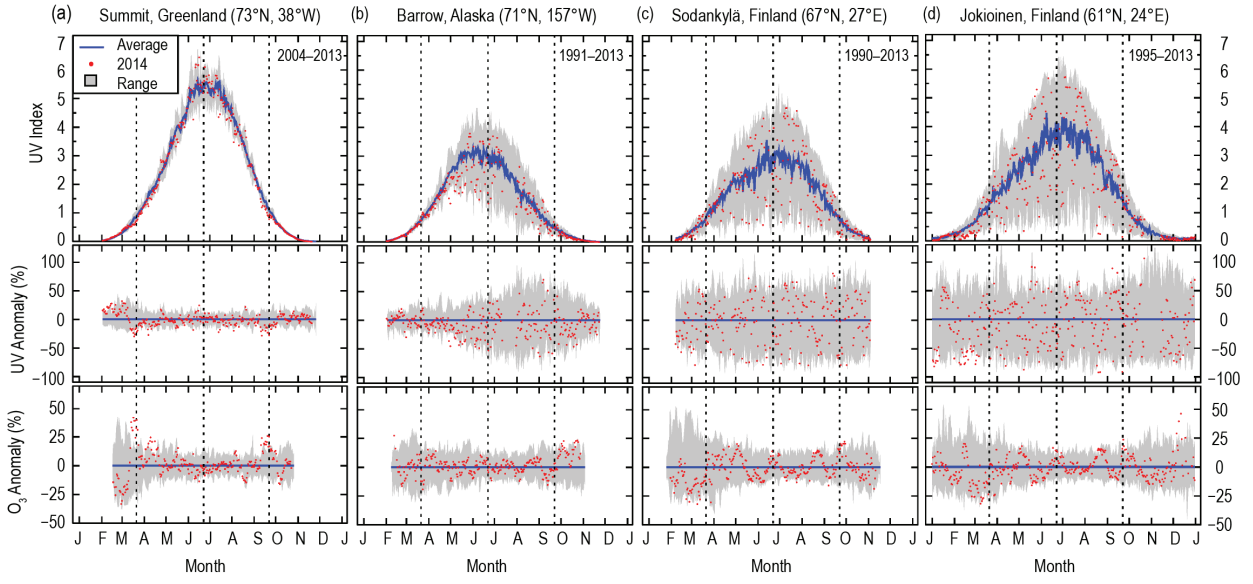

Fig. 5.8. Seasonal variation of the UV index (UVI) measured by ground-based radiometers at (a) Summit, Greenland, (b) Barrow, Alaska, (c) Sodankylä, Finland, and (d) Jokioinen, Finland. Data are based on the UVI averaged over a period of two hours centered at solar noon. The top panel for each site compares UVI in 2014 (red dots) with the average noon UVI (blue line), and the range of historical minima and maxima (shading). Average and ranges of both UV and ozone data were calculated from measurements of the years of available UV data indicated in the top right corner of each UVI panel. The center horizontal panel shows the relative UVI anomaly calculated as the percentage departure from the climatological mean. The bottom panel shows a similar anomaly analysis for total ozone derived from measurements from satellites during the period (http://avdc.gsfc.nasa.gov/index.php?site=1593048672&id=28 and http://ozoneaq.gsfc.nasa.gov). Vertical broken lines indicate the times of the vernal equinox, summer solstice, and autumnal equinox, respectively.

because the transition from highly reflective snow cover to the low albedo of snow-free ground is coupled with increasing solar radiation during the lengthening days of the high-latitude spring.

Snow cover extent (SCE) anomalies for spring (April–June) 2014 were computed separately for North American and Eurasian sectors of the Arctic from the satellite-derived weekly NOAA snow chart climate data record (CDR; maintained at Rutgers University; described in Brown and Robinson 2011 and Estilow et al. 2013). Below-normal SCE with respect to the 1981–2010 reference period was observed for each month and region, with the exception of North America in April (Fig. 5.9a). This is consistent with a previous analysis that identified a dramatic loss of Northern Hemisphere spring SCE over the past decade (Derksen and Brown 2012).

In 2014, a new record low April SCE for the satellite era was established for Eurasia, driven by strong positive surface temperature anomalies over eastern Eurasia (see Fig. 5.2) and anomalously shallow snow depth over western Eurasia and northern Europe (Fig. 5.9d). The low snow accumulation across Europe and western Russia was consistent with warm temperature anomalies and reduced precipitation associated with the positive phase of the East Atlantic (EA) teleconnection pattern, which was strongly positive (mean index value of 1.43) from December 2013 through March 2014 (www.cpc.ncep.noaa.gov/data/teledoc/ea.shtml).

Across North America, April SCE was above average (standardized anomaly of 0.86) as colder-than-normal surface temperatures extended across the Canadian Arctic and subarctic. Temperature anomalies shifted to positive in some regions during May (particularly in a dipole pattern over the eastern Canadian Arctic and Alaska), and were extensively warmer than average by June. This drove June SCE in North America to the third lowest in the satellite record in spite of the positive SCE anomalies in April.

For both the North American and Eurasian sectors of the Arctic, below-average SCE was observed during May for the ninth time in the past ten spring seasons, and for the tenth consecutive June. Evidence

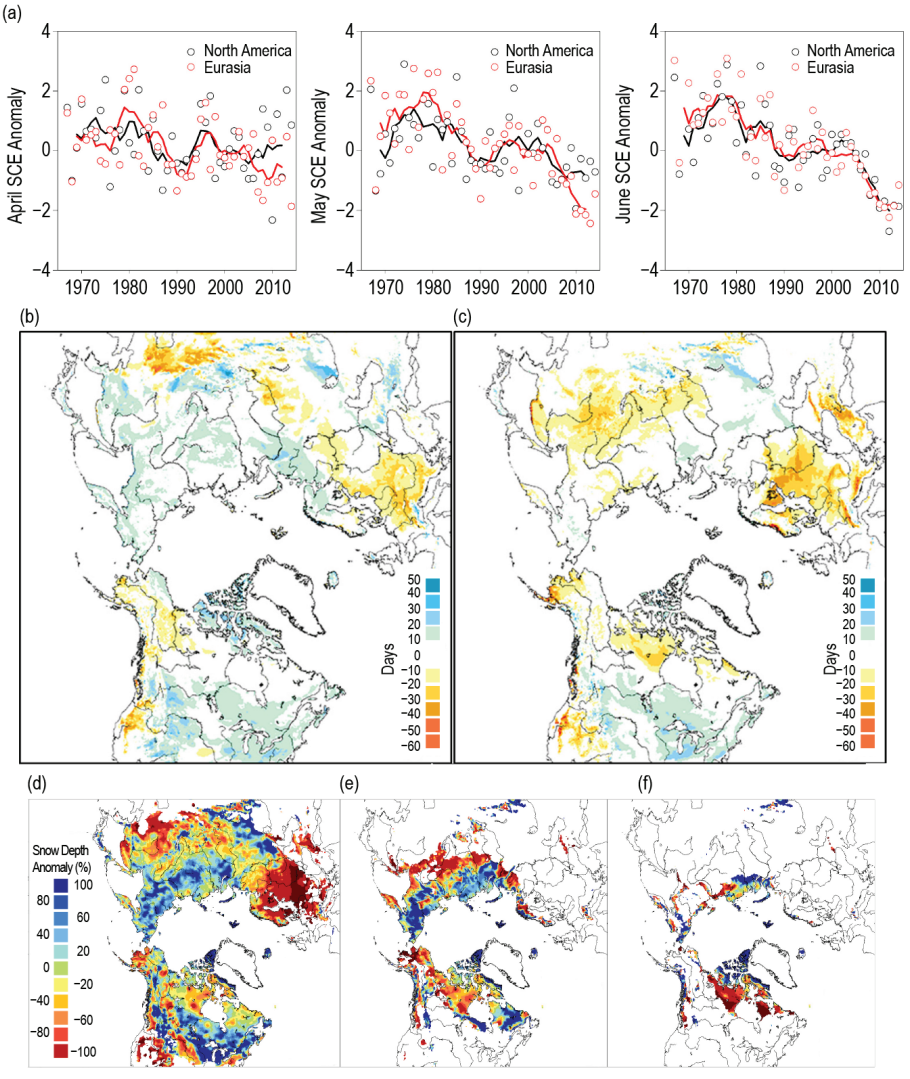

Fig. 5.9. Arctic snow cover extent standardized (unitless) anomaly time series (with respect to 1988–2007) from the NOAA snow chart CDR for (a) Apr, May, and Jun 1967–2014 (solid lines denote 5-yr moving average); Snow cover duration departures (with respect to 1998–2010) from the NOAA IMS data record for the (b) 2013 fall and (c) 2014 spring seasons; snow depth anomaly (% of 1999–2010 average) from the CMC snow depth analysis for (d) Apr, (e) May, and (f) Jun 2014. (Source: Arctic Report Card: Update for 2014, http://arctic.noaa.gov/reportcard/snow_cover.html.)

is emerging that Arctic warming is driving synchronous pan-Arctic responses in the terrestrial and marine cryosphere; reductions in May and June SCE (–7.3% and –19.8% decade^{-1}, respectively) bracket the rate of September sea ice loss (–13.3% decade^{-1}) over the 1979–2014 period for which satellite-derived sea ice extent is available (see section 5i).

As discussed in the *Arctic Report Card: Update for 2014* (http://arctic.noaa.gov/reportcard/snow_cover.html), snow cover duration (SCD) departures derived from the NOAA daily Interactive Multisensor Snow and Ice Mapping System (IMS) snow cover product (Helfrich et al. 2007) show snow cover onset 10–20 days earlier than average (with respect to 1998–2010) across northwestern Russia, northern Scandinavia, the Canadian Arctic Archipelago, and the North Slope of Alaska, with later snow onset over northern Europe and the Mackenzie River region in northwestern Canada (Fig. 5.9b). The spring SCD departures (Fig. 5.9c) are consistent with the April snow depth anomaly pattern [(Fig. 5.9d; derived from the Canadian Meteorological Centre (CMC) daily gridded global snow depth analysis described in Brasnett 1999)] with below-normal snowpack and 20–30 day earlier melt over northern Europe, Siberia, and the central Canadian Arctic. Above-normal snow depths were observed during early spring over much of northern Russia but did not translate into later-than-normal spring snow cover due to above-normal spring temperatures that contributed to rapid ablation (Fig. 5.9d,e). This finding is consistent with the observation of Bulygina et al. (2010) of a trend toward increased winter snow accumulation and a shorter, more intense spring melt period over large regions of Russia.

e. *Glaciers and ice caps outside Greenland*—M. Sharp, G. Wolken, D. Burgess, J. G. Cogley, L. Copland, L. Thomson, A. Arendt, B. Wouters, J. Kohler, L. M. Andreassen, S. O'Neel, and M. Pelto

Mountain glaciers and ice caps cover an area of over 400 000 km^2 in the Arctic, and are a major influence on global sea level (Gardner et al. 2011, 2013; Jacob et al. 2012). They gain mass by snow accumulation and lose mass by meltwater runoff. Where they terminate in water (ocean or lake), they also lose mass by iceberg calving. The climatic mass balance (B_{clim}, the difference between annual snow accumulation and annual meltwater runoff) is a widely used index of how glaciers respond to climate variability and change. The total mass balance (ΔM) is defined as the difference between annual snow accumulation and annual mass losses (by iceberg calving plus runoff).

The World Glacier Monitoring Service (WGMS) maintains the B_{clim} records of 27 glaciers. Data for these glaciers are submitted by national correspondents of the WGMS. As B_{clim} measurements for mass balance year 2013/14 are available for only 12 of the 27 glaciers that are monitored across the Arctic (three each in Alaska, Iceland, Norway, and Svalbard), and some of these are still provisional, this report section focuses primarily on the 24 glaciers for which 2012/13 measurements are available (WGMS 2015). Those glaciers are located in Alaska (three), Arctic Canada (four), Iceland (nine), Svalbard (four) and northern Scandinavia (four) (Fig. 5.10; Table 5.1). For these glaciers as a group, the mean B_{clim} in 2012/13 was negative. However, five glaciers had positive balances: Devon Ice Cap, Meighen Ice Cap, and White Glacier in Arctic Canada; Hofsjökull SW in Iceland; and Hansbreen in Svalbard.

For the Arctic as a whole, 2012/13 was the eleventh most negative mass balance year since records began in 1946, and the sixth most negative year since 1989. At least 20 Arctic glaciers have been measured each

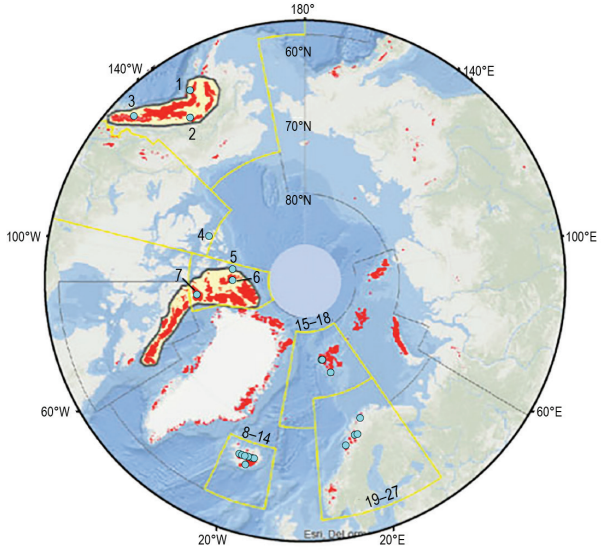

Fig. 5.10. Locations (light blue circles) of 27 Arctic glaciers with long-term records of annual climatic mass balance (B_{clim}). See Table 5.1 for glacier names. Regions outlined in yellow are the Randolph Glacier Inventory (RGI) regions for major regions of the Arctic. In regions where individual glaciers are located too close together to be identifiable on the map, their numbers are shown at the edge of the RGI region in which they occur. Red shading indicates glaciers and ice caps, including ice caps in Greenland outside the ice sheet. Yellow shading shows the solution domains for regional mass balance estimates for the Canadian Arctic and Gulf of Alaska regions derived using gravity data from the GRACE satellites (see Fig. 5.12).

Table 5.1. Measured annual climatic mass balance (B_{clim}) of glaciers in Alaska, Arctic Canada, Iceland, Svalbard, and northern Scandinavia for 2012/13 and 2013/14, together with the mean and standard deviation for each glacier for the period 1980–2010. Numbers in column 1 identify glacier locations in Fig. 5.10. Mass balance data are from the World Glacier Monitoring Service, with corrections to Svalbard data provided by J. Kohler and to Alaska data provided by S. O'Neel. The 2013/14 data for Langfjordjøkelen and all data for Rundvassbreen were provided by L. Andreassen. Note that 2013/14 results may be based upon data collected before the end of the 2014 melt season and may be subject to revision.

Region	Glacier (Record length, years)	Mean Climatic Balance 1980–2010 (kg m^{-2} yr^{-1})	Standard Deviation of Climatic Mass balance 1980–2010 (kg m^{-2} yr^{-1})	Climatic Balance 2012–13 (kg m^{-2} yr^{-1})	Climatic Balance 2013–14 (kg m^{-2} yr^{-1})
Alaska					
1	Wolverine (49)	−285	1205	−2250	−1400
3	Lemon Creek (62)	−584	709	−750	−1825
2	Gulkana (49)	−505	738	−1190	−80
Arctic Canada					
7	Devon Ice Cap (53)	−153	176	+24	
5	Meighen Ice Cap (52)	−173	284	+160	
4	Melville South Ice Cap (51)	−295	369	−172	
6	White (51)	−239	260	+45	
Iceland					
8	Langjökull S. Dome (17)	−1448	817	−851	
9	Hofsjökull E (24)	−602	1009	−440	−990
9	Hofsjökull N (25)	−606	787	−360	−950
9	Hofsjökull SW (24)	−978	947	+60	−990
14	Köldukvislarjökull (21)	−529	738	−560	
10	Tungnaarjökull (22)	−1170	873	−810	
13	Dyngjujökull (16)	−133	912	−230	
12	Brúarjökull (21)	−367	660	−70	
11	Eyjabakkajökull (22)	−867	813	−500	
Svalbard					
17	Midre Lovenbreen (47)	−356	305	−940	+50
16	Austre Broggerbreen (48)	−469	342	−1090	+10
15	Kongsvegen (28)	−70	378	−690	+116
18	Hansbreen (25)	−431	512	+143	
Northern Scandinavia					
20	Engabreen (41)	+463	1091	−1779	−890
21	Langfjordjøkelen (24)	−927	781	−2615	−780
22	Marmaglaciaren (23)	−430	525		
23	Rabots Glaciar (29)	−394	560		
24	Riukojietna (26)	−592	805		
25	Storglaciaren (68)	−113	698	−1406	
26	Tarfalaglaciaren (18)	−212	1101		
27	Rundvassbreen (7)	−777		−2430	−790

year since 1989. For the three Canadian glaciers with positive 2012/13 climatic balances, the balances were among the 7–13 most positive since measurements began in 1960. Only nine years since 1960 have had positive measured glacier climatic balance in Arctic Canada; 2012/13 was only the second since 1986.

The 2012/13 positive balances of Arctic Canada glaciers were most likely linked to melt suppression by anomalously cool temperatures over the Canadian Arctic Islands in summer 2013, when June–August mean air temperatures at 850 hPa were 0.5°–2.5°C below the 1981–2010 mean, according to

the NCEP-NCAR R1 Reanalysis (Kalnay et al. 1996). By contrast, near-record negative 2012/13 climatic balances in northern Scandinavia coincided with June–August 850-hPa air temperatures 1.0°–2.5°C above the 1981–2010 mean. Strongly negative climatic balances in Alaska and Svalbard were also linked to positive 850-hPa air temperature anomalies in these regions in summer 2013. The positive and negative near-surface air temperature anomalies described here are illustrated in Overland et al. (2013, 2014b).

Among the 12 glaciers for which the 2013/14 climatic balances have been reported (Table 5.1), Svalbard glacier balances were all positive, while those in Alaska, Norway, and Iceland were all negative. Local observations suggest that the positive balances in Svalbard were attributable to high winter precipitation, especially at low elevations, followed by a relatively cool summer. On the other hand, Alaska, northern Scandinavia, and Iceland all had positive 850-hPa air temperature anomalies in July–September 2014, exceeding +2.5°C in parts of northern Norway and Sweden, according to NCEP/NCAR R1 (Overland et al. 2014b). In Norway, 2014 was the warmest year on record (2.2°C above the 1961–90 mean) and temperatures in July were 4.3°C above the long-term mean.

Cumulative regional climatic mass balances, derived by summing the annual mean climatic mass balances for all glaciers in each reporting region of the Arctic, have become increasingly negative over the past two decades (Fig. 5.11). These negative trends are also evident in regional total mass balance estimates (ΔM) for the heavily glaciated regions of Arctic Canada and Alaska derived using GRACE satellite gravimetry (Fig. 5.12). Measurements of ΔM for all the glaciers and ice caps in Arctic Canada clearly show a negative mass balance year in that region in 2013/14, as do measurements for Alaska. Since summer air temperatures over Arctic Canada were not unusually warm in 2014, the negative mass balance there may be linked to the relatively low snow accumulation in winter 2013/14 that is apparent in the GRACE data. In Alaska, however, anomalously warm (up to +1.0°C) summer temperatures in 2014 were likely a factor in that region's negative balance.

f. Greenland Ice Sheet—M. Tedesco, J. E. Box, J. Cappelen, X. Fettweis, T. Mote, R. S. W. van de Wal, M. van den Broeke, C. J. P. P. Smeets, and J. Wahr

Melt extent for the period June–August (JJA, "summer" or melt season) 2014, estimated from microwave brightness temperatures measured by the Special Sensor Microwave Imager/Sounder (SSMI/S; e.g., Mote 2007; Tedesco et al. 2013a,b), was above

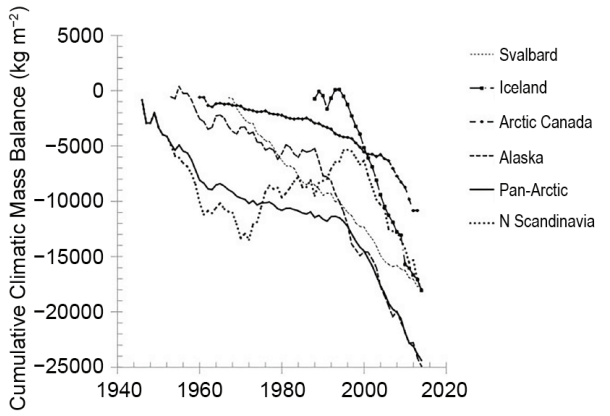

Fig. 5.11. Cumulative climatic mass balances (B_{clim} in kg m^{-2}) for glaciers in five regions of the Arctic, and for the Arctic as a whole (Pan-Arctic). Mean balances are calculated for glaciers monitored in each region in each year and these means are cumulated over the period of record. Note that the period of monitoring varies between regions and that the number and identity of glaciers monitored in a given region may vary between years.

the 1981–2010 average 90% of the time (83 of 92 days; Fig. 5.13a), with positive anomalies reaching maximum values along the western ice sheet.

The number of days of surface melting in June and July 2014 exceeded the 1981–2010 average over most of the ice sheet, particularly along the southwestern margin (Fig. 5.13b), the latter consistent with the anomalously high temperatures recorded at coastal stations in western Greenland during that period (Tedesco et al. 2014). The number of days of surface melting was also particularly high on the northeastern margin of the ice sheet

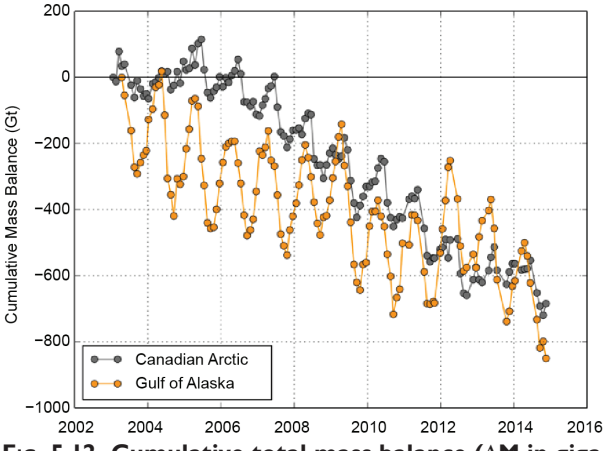

Fig. 5.12. Cumulative total mass balance (ΔM in gigatonnes, Gt) of glaciers in the Canadian Arctic and the Gulf of Alaska region for 2003–15. The uncertainty of the calculated mass balances is ±8 Gt yr^{-1} for the Gulf of Alaska and ±9 Gt yr^{-1} for the Canadian Arctic. This includes the formal error of the least squares fit and the uncertainties in the corrections for glacial isostatic adjustment, Little Ice Age, and hydrology.

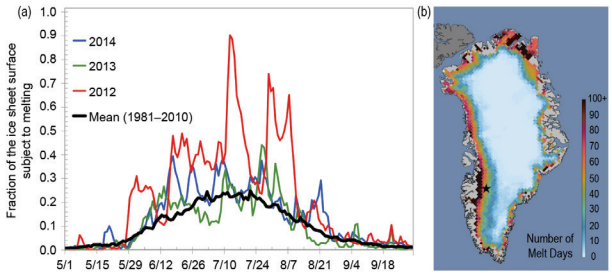

Fig. 5.13. Melting on the Greenland Ice Sheet in 2014 as described by (a) daily values of the fraction of the ice sheet subject to melting, and (b) total number of days when melting was detected between 1 Jan and 1 Oct 2014. In (a) melt extent in 2014 is represented by the blue line and the long-term average is represented by the black line. The black star in (b) indicates the position of the K-transect described in the surface mass balance paragraph.

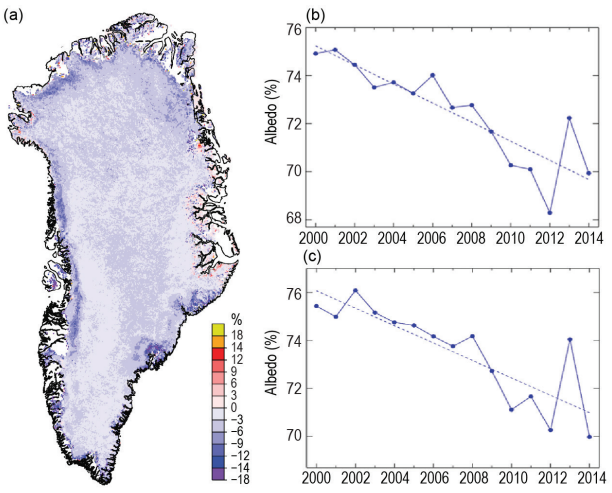

Fig. 5.14. (a) Greenland Ice Sheet surface albedo anomaly for Jun–Aug 2014 relative to the average for those months between 2000 and 2011. (b) Average surface albedo of the whole ice sheet each summer since 2000. (c) Average surface albedo of the ice sheet each August since 2000. All data are derived from the MODIS bands 1–7 (updated from Box et al. 2012).

(Fig. 5.13b). There was a below-average number of days of melting in southeast Greenland, consistent with below-normal temperatures in that region (Tedesco et al. 2014).

Melting occurred over 4.3% more of the ice sheet, on average, than in summer 2013, but 12.8% less than the exceptional summer of 2012, when record melt extent occurred. The melt extent maximum of 39.3% of the total ice sheet area on 17 June 2014 (Fig. 5.13a), and similar values on 9 July and 26 July, exceeded the 1981–2010 average by two standard deviations. Melt extent exceeded the 1981–2010 average for 28 days in June, 25 days in July, and 20 days in August 2014. For a brief period in early August there was below-average melt extent, but by 21 August melting occurred on 29.3% of the ice sheet (Fig. 5.13a); this exceeded the 1981–2010 average by two standard deviations.

In summer 2014, albedo, derived from the Moderate-resolution Imaging Spectroradiometer (MODIS), was below the 2000–11 average over most of the ice sheet (Fig. 5.14a) and the area-averaged albedo for all Greenland ice was the second lowest in the period of record since 2000 (Fig. 5.14b). (MODIS observations began in 2000; hence the use of the reference period 2000–11 rather than 1981–2010 to calculate albedo anomalies.) The area-averaged albedo in August was the lowest on record for that month (Fig. 5.14c). August 2014 albedo values were anomalously low at high elevations; such low values have not previously been observed so late in the summer. Overall, the albedo in summer 2014 continued the period of increasingly negative and record low albedo anomaly values since observations began in 2000 (Box et al. 2012; Tedesco et al. 2011, 2013a).

The climatic mass balance (B_{clim}, the difference between annual snow accumulation and annual meltwater runoff, see section 5e) measured along the K-transect (Fig. 5.13b, black star) in west Greenland (Van de Wal et al. 2005, 2012) for September 2013 through September 2014 was slightly below the average for 1990–2010 (measurements began in 1990). The equilibrium line altitude (the lowest altitude at which winter snow survives) was estimated to be at 1730 m above sea level (a.s.l.) in 2014, above the 1990–2010 mean (1550 m) but below the exceptional values estimated in 2012 (above 2000 m). The K-transect observations are broadly consistent with the anomalously high near-surface air temperatures measured along the west Greenland coast.

The change in total mass balance (ΔM, see section 5e) estimated by the GRACE (Gravity Recovery and Climate Experiment; Velicogna and Wahr 2006) satellite (Fig. 5.15) indicates a net mass loss of 220 Gt (gigatonnes) between the beginning of October 2013 and the beginning of October 2014. This is lower than the average October-to-October mass loss of 269 Gt during 2003–13.

The spatial extent and number of days of melting, particularly the high values in west Greenland, and the K-transect mass balance observations occurred in a summer with a negative (−0.7) North Atlantic Oscillation (NAO). This NAO promoted anticyclonic circulation conditions over southwest and northwest Greenland and advection of warm southerly air along its western margin as far as the northern regions of the ice sheet (Tedesco et al. 2014). As a consequence, high near-surface air temperatures occurred at weather stations in west Greenland. For example, summer

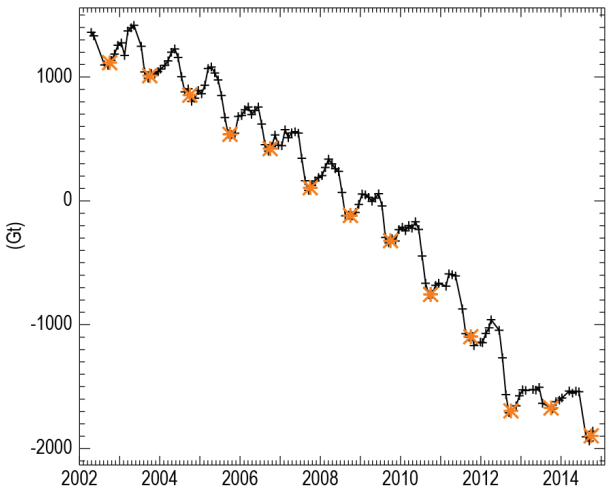

Fig. 5.15. Cumulative total mass balance (ΔM in gigatonnes, Gt) of the Greenland Ice Sheet since Apr 2002, estimated from GRACE measurements. The orange asterisks are for reference and denote the GRACE values interpolated to 1 October each year.

2014 was the warmest since measurements began in 1949 at Kangerlussuaq (relative to the 1981–2010 average, the June–August temperature anomaly was +1.6°C, with a June anomaly of +2.3°C), and the second warmest (together with summer 2010) since 1784 at Nuuk (the June–August anomaly was +2.3°C, with a July anomaly of +2.9°C).

g. Terrestrial permafrost—V. E. Romanovsky, S. L. Smith, H. H. Christiansen, N. I. Shiklomanov, D. A. Streletskiy, D. S. Drozdov, G. V. Malkova, N. G. Oberman, A. L. Kholodov, and S. S. Marchenko

Permafrost is defined as soil, rock, and any other subsurface earth material that exists at or below 0°C for two or more consecutive years. On top of the permafrost is the active layer, which thaws during the summer and freezes again the following winter. The mean annual temperature of permafrost and the thickness of the active layer are good indicators of changing climate. Changes in permafrost temperatures and active layer thickness in Alaska, Canada, Russia, and the Nordic region are reported here.

Permafrost temperature (at depths of 10–200 m) is a sensitive indicator of the decade-to-century climate variability and long-term changes in the surface energy balance. This is because the range of the interannual temperature variations ("noise") decreases rapidly with depth, while decadal and longer time-scale variations ("signal") penetrate to greater depths in the permafrost with less attenuation. Consequently, the "signal-to-noise" ratio increases rapidly with depth and the ground acts as a natural low-pass filter of the climatic signal, making temperature-depth profiles in permafrost useful for studying past temperature changes at the ground surface. Increasing permafrost temperatures and active layer thickness caused by climate warming affect the stability of northern ecosystems and infrastructure, and are predicted to cause the release of carbon into the atmosphere in the form of the greenhouse gases carbon dioxide and methane.

In 2014, new record high temperatures at 20-m depth were measured at all permafrost observatories on the North Slope of Alaska (hereafter North Slope), except for the Happy Valley site (Fig. 5.16a,b). Changes in permafrost temperatures at 20-m depth typically lag about one year behind the changes in surface temperatures. The summer of 2013 was particularly warm on the North Slope and thus contributed to the 20-m temperature increase. The permafrost temperature increase in 2014 was substantial; 20-m temperatures in 2014 were 0.07°C higher than in 2013 at West Dock and Deadhorse, and 0.06°C higher at Franklin Bluffs (Fig. 5.16b) on the North Slope. A 0.09°C increase was observed at Galbraith Lake (Fig. 5.16b) in the northern foothills of the Brooks Range. Permafrost temperature in 2014 at Happy Valley was 0.03°C higher than in 2013, but still 0.03°C lower than the record maximum set in 2012. Temperature at 20-m depth has increased between 0.18° and 0.56°C decade^{-1} since 2000 on the North Slope (Fig. 5.16b).

Permafrost temperatures in Interior Alaska generally continued to decrease slightly in 2014 (Fig. 5.16c), a cooling that dates back to 2007. Consequently, temperatures in 2014 at some sites in Interior Alaska were lower than those located much farther north, for example, temperatures at College Peat are now lower than at Old Man (Fig. 5.16c). However, at two sites, Birch Lake and Healy, this cooling trend was interrupted in 2014 by a warming of 0.1°C and 0.05°C, respectively (Fig. 5.16c).

In 2013/14, temperatures in the upper 25 m of ground at Alert, northernmost Ellesmere Island, Canada, were among the highest recorded since 1978, but have remained stable at 24-m depth for the past two years while a slight cooling is observed at 15-m depth (Fig. 5.17). At Alert BH5, temperature at 15-m depth has increased by ~1.3°C decade^{-1} since 2000, which is about 0.8°C decade^{-1} higher than the rate for the entire record. Even at a depth of 24 m, temperature at the Alert BH1 and BH2 sites has increased since 2000 at a rate approaching 1°C decade^{-1}. The slower rate of temperature increase at 24-m depth and the slight cooling at 15-m depth over the last two years is likely a response to a decrease in air temperatures between 2010 and 2013.

A similar pattern is observed in the shorter records from eastern Arctic sites, where permafrost tempera-

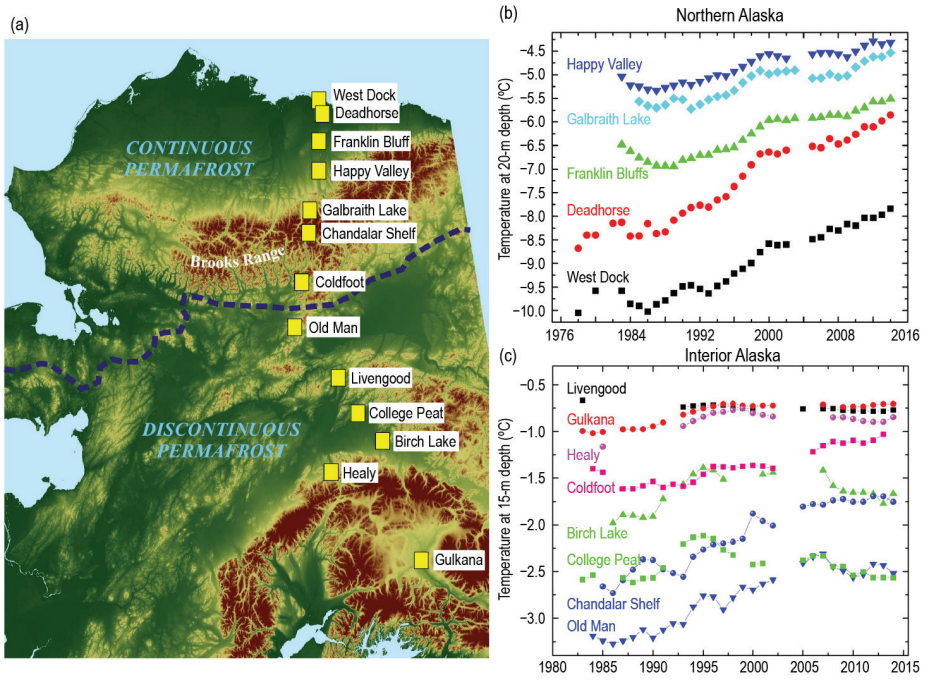

Fig. 5.16 (a) Continuous and discontinuous permafrost zones in Alaska (separated by the broken blue line) and location of a north–south transect of permafrost temperature measurement sites; (b) and (c) time series of mean annual temperature (°C) at depths of 20 m and 15 m below the surface, respectively, at the measurement sites (updated from Romanovsky et al. 2014).

tures at 15-m depth have increased between 2008 and 2013 (Fig. 5.17). Temperatures in the warm permafrost of the central Mackenzie River valley in northwestern Canada continue to increase, but at a much slower rate than in the high Arctic, and which has slowed further in the last decade (Fig. 5.17). At depths of 10–12 m, the permafrost temperature at Norman Wells and Wrigley has risen by 0.01°–0.2°C decade^{-1} since 2000. Permafrost temperatures measured since 2007 at 8.75-m depth in the northern Mackenzie Valley near Inuvik have increased by about 0.4°C decade^{-1}.

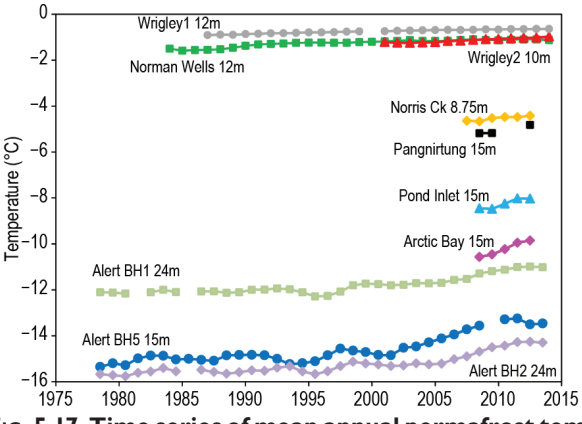

Fig. 5.17. Time series of mean annual permafrost temperatures in Arctic Canada: in the discontinuous, warm permafrost of the central Mackenzie River Valley, Northwest Territories (Norman Wells and Wrigley); in the northern Mackenzie Valley near Inuvik (Norris Ck); in continuous, cold permafrost at Alert, Nunavut; in the eastern Arctic (Pangnirtung, Pond Inlet, Arctic Bay) (updated from Smith et al. 2010, 2012). Depths of measurement are indicated in the graph. The method described in Smith et al. (2012) was used to address gaps in the data and produce a standardized record of mean annual ground temperature.

Permafrost temperature has increased by 1°–2°C in northern Russia during the last 30 to 35 years (Romanovsky et al. 2010), similar to the increase observed in northern Alaska and the Canadian high Arctic. In the European north of Russia and in the western Siberian Arctic, for example, temperatures at 10-m depth have increased by ~0.4°C to 0.6°C decade^{-1} since the late 1980s at colder permafrost sites (Fig. 5.18, Bolvansky #59, Urengoy #15-5, and Urengoy #15-10). Less warming has been observed at warm permafrost sites in both regions (Fig. 5.18, sites Bolvansky #56 and Urengoy #15-6).

Limited long-term permafrost temperature records for the Nordic area indicate increases since the late 1990s of 0.4°–0.7°C decade^{-1} in the highlands of southern Norway, northern Sweden, and Svalbard, with the largest warming in Svalbard and in northern Scandinavia (Isaksen et al. 2011; Christiansen et al. 2010). New sites established in Greenland are providing new information on the thermal state of permafrost. In western Greenland, permafrost temperatures are relatively warm, from –1°C to –3°C (Christiansen et al. 2010). In eastern Greenland, at Zackenberg Research Station, permafrost temperature at 18-m depth was –6.8°C within a flat open area and –5.8°C at a snowdrift site, based on the two-year record collected in summer 2014. At the new Villum Research Station at Station Nord in north Greenland, the temperature measured in August 2014 at 20-m depth was –8.2°C.

Decadal trends in the active layer thickness (ALT) vary by region (Shiklomanov et al. 2012). In 2014, sites on the Alaska North Slope reported lower ALT values

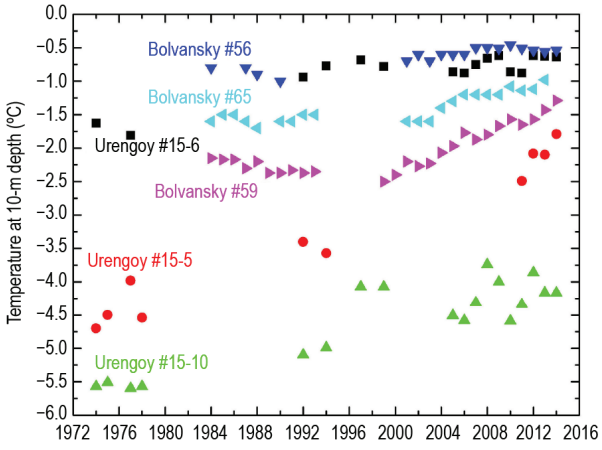

Fig. 5.18. Time series of mean annual permafrost temperatures (°C) at 10-m depth at six research sites in the European north of Russia (Bolvansky #56, 59, and 65) and in the western Siberian Arctic (Urengoy #15-5, 15-6, and 15-10).

than in 2013 (Fig. 5.19). Out of 28 observational sites in northern Alaska, only one, located on the Seward Peninsula, reported a slight increase in the ALT in 2014. The average ALT in 2014 for the 20 North Slope sites with a long (≥10 years) observational record was 0.48 m, similar to the 1995–2013 average of 0.47 m. In the interior of Alaska, however, ALT increased substantially in 2014; three of the four sites reported the highest 2014 ALT values in the 1995–2014 observational record.

Records from 25 sites with thaw tubes in the Mackenzie Valley, northwestern Canada, indicate that ALT in 2013 (the most recent year data are available) was greater than the 2002–12 average for most sites (Duchesne et al. 2014). In this region ALT has generally increased since 2008, although in 2013 it was slightly less than in 2012, which was on average about 10% greater than the long-term mean (Fig 5.19).

In Russia, standardized active layer observations in 2014 were conducted at 36 sites. A decrease in ALT in 2014 was observed in west Siberia (Fig. 5.19). Out of the eight West Siberian sites that reported data in 2014, only three, located in the southernmost part of the region, have a substantial (0.6–0.22 m) increase in ALT. The other five sites reported 0.08–0.15 m ALT decreases. Locations in the Russian European North have been characterized by almost monotonic thickening of the active layer over the last 15 years and reached a record maximum in 2012. However, in 2014, all four sites within the region reported a decrease in ALT ranging from 0.02 to 0.22 m compared to 2013 (Fig. 5.19). In north central Siberia, ALT increased by 0.07–0.09 m, while ALT in the center of the region (Yakutsk) was largely unchanged. Sites in south central Siberia reported a 0.10–0.13 m decrease in ALT in 2014, while in eastern Siberia ALT in 2014 increased by an average of 8% compared to 2013, and only 4 out of 17 sites reported a slight decrease in ALT. In 2014, ALT in Chukotka (Russian Far East) was about 2% higher than in 2013, marking a slight increase during 2011–14 that reversed a sharp decline in 2008–10 (Fig. 5.19).

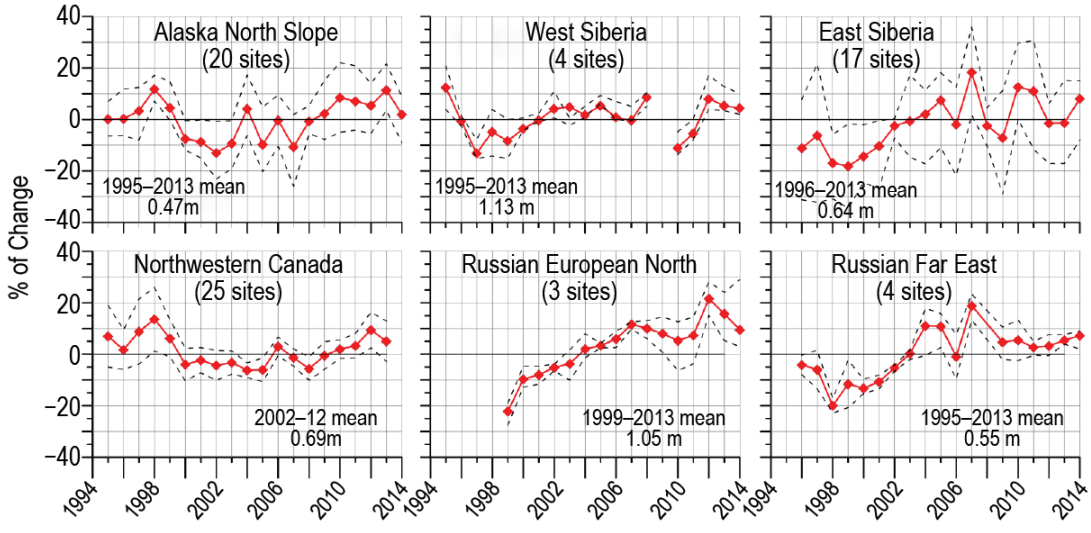

Fig. 5.19. Long-term active-layer change in six different Arctic regions as observed by the Circumpolar Active Layer Monitoring project. The data are presented as annual percentage deviations from the mean value for the period of observations. Thaw depth observations from the end of the thawing season were used. Only sites with at least 10 years of continuous thaw depth observations are shown. Solid red lines show mean values; dashed black lines represent maximum and minimum values.

SIDEBAR 5.2: DECLASSIFIED HIGH-RESOLUTION VISIBLE IMAGERY FOR OBSERVING THE ARCTIC—H. E. EPSTEIN, G. V. FROST, D. A. WALKER, AND R. KWOK

There has been widespread use of remote sensing for Arctic research with satellite and sensor platforms dating back to the early 1970s, beginning with the NASA Earth Resources Technology Satellite (later renamed Landsat) and NOAA satellite missions. These and many other satellite-derived data have generally been widely available for scientific, commercial, and educational applications. Less well known, however, is imagery that was originally obtained for national security purposes by the broadly defined U.S. intelligence community, and then later declassified for scientific use. Here, some results of Arctic terrestrial vegetation and sea ice research that used declassified imagery obtained by Corona/Gambit and National Technical Means satellite missions are described.

Corona/Gambit and Arctic tundra vegetation

Corona was the first operational U.S. satellite program designed for photographic reconnaissance from space. Based on prior satellite programs implemented by the U.S. Air Force and approved by President Eisenhower in 1958, Corona operations were conducted by the Air Force, but image retrieval was under the direction of the Central Intelligence Agency (CIA). The first successful Corona mission, carrying the KeyHole (KH-1) camera, was launched in 1960. In 1961, Secretary of Defense McNamara and CIA Director Dulles established the National Reconnaissance Office (NRO) which oversaw the Corona mission under the co-direction of the Air Force and the CIA. Corona was intended to be a short-term mission that would be succeeded by other more strategic efforts, but it ran until 1972, collecting images at resolutions as fine as 1.8 m (Berkowitz 2011).

The Gambit program, with vehicle, camera, film, and retrieval specifications different than those for Corona, had its origins in 1960, even before the first successful Corona mission (Oder et al. 2012). Gambit missions ran from 1963 to 1967, with the KH-7 camera system, imaging primarily China and the Soviet Union at resolutions less than 1.2 m and as fine as 0.6 m.

Corona imagery was declassified in 1995 under an Executive Order signed by President Clinton, and the same order dictated the declassification of Gambit photographs in 2002. Declassified Corona images are available at https://lta.cr.usgs.gov/declass_1, and Gambit images are available at https://lta.cr.usgs.gov/declass_2.

Several recent studies have used declassified Corona and Gambit imagery to observe and evaluate the expansion of tall shrubs and trees along the forest-tundra ecotone of Siberia over the past 4–5 decades (Frost et al. 2013, 2014; Frost and Epstein 2014). Corona and Gambit panchromatic imagery from 1965 to 1969 were paired with recent high-resolution imagery from various commercial sensors (IKONOS, Quickbird, Geo-Eye-1, and WorldView-1 and -2) from 2002 to 2011 to examine the vegetation change at 11 sites throughout the southern tundra of Russia.

The 1960s and the 21st century images allow for the clear distinction of tall shrubs (alder, willow, and dwarf pine) from the shorter-statured tundra dominated by sedges and mosses (Fig. SB5.2). The imagery also facilitates the detection of individual larch trees, as their shadows

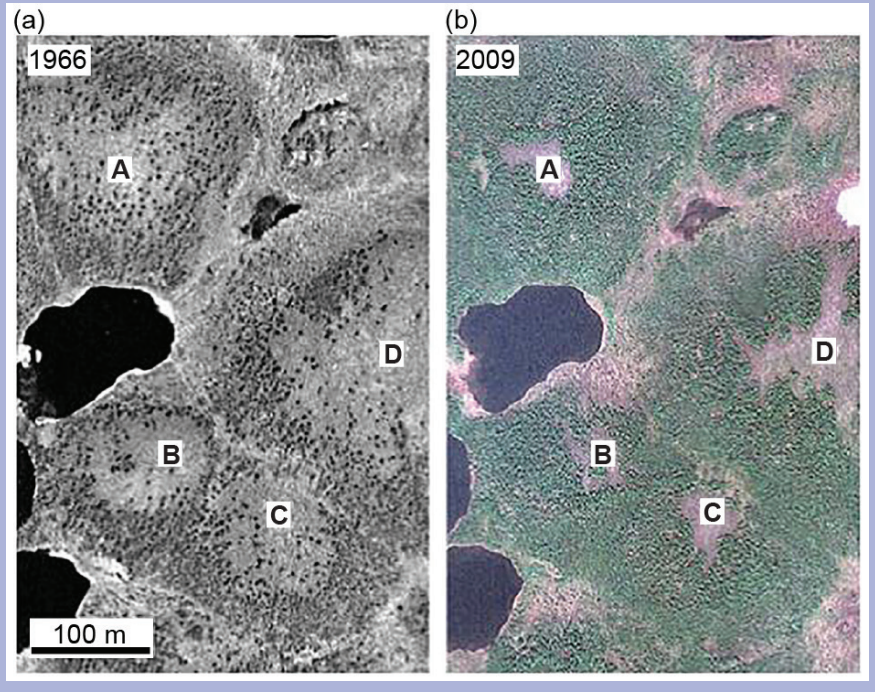

Fig. SB5.2. Comparison of 1966 Gambit (left) and 2009 GeoEye-1 (right) images showing alder expansion at Dudinka, northwest Siberia. (Source: Frost and Epstein 2014.) Letters A, B, C, and D identify the same sites in each image.

are clearly apparent due to low sun angles at these high latitudes. Frost and Epstein (2014) found that tall shrubs and trees had expanded by up to 26% over these landscapes since the 1960s. Only one site showed a slight decline in tall shrubs and another a decline in larch, largely due to flooding and thermokarst disturbances. This was one of the first studies to observe widespread increases in tall shrubs in upland tundra (as opposed to riparian) ecosystems.

MEDEA and Arctic sea ice

In 1995, the MEDEA (Measurements of Earth Data for Environmental Analysis) group was appointed to advise the U.S. government on the acquisition of imagery over geophysically interesting targets that take advantage of the unique capabilities of classified National Technical Means (NTM). The sites are designated "fiducial sites" to suggest that the imagery record, if made available to the science community, would be of potential value for establishing historical baselines for understanding recent changes in the environment. A National Research Council report (NRC 2009) that coincided with the first data release and a recent article (Kwok 2014a) discuss the potential scientific value and utility of continued acquisition of NTM imagery for arctic research.

Since 1995, periodic image acquisitions over the fiducial sites have continued; the Global Fiducials Library (http://gfl.usgs.gov) is the long-term repository of the datasets, maintained by the U.S. Geological Survey. The USGS has released thousands of declassified NTM images acquired since 1999 with 1-m resolution in the visible-band, referred to as Literal Image Derived Products (LIDPs), at six fixed fiducial sites around the Arctic basin. These static sites include: Beaufort Sea, Canadian Arctic, Fram Strait, East Siberian Sea, Chukchi Sea, and Point Barrow. When cloud cover allows, weekly coverage is available between April and September. In the LIDPs, meter-scale features on drifting ice floes (e.g., melt ponds, ridges, fractures, leads, etc.), important for studying small-scale arctic sea ice processes, are resolvable. To illustrate, Fetterer et al. (2008) used LIDPs to determine statistics for melt pond size and areal coverage.

More recently, a new mode of targeted data acquisition, guided by the coordinates from drifting buoys, provides the capability to trace the evolution of surface conditions (e.g., melting) on the same ice floes through the summer (Fig. SB5.3). This "Lagrangian" mode of acquisition has proven to be invaluable for making observations over the drifting sea ice cover. LIDPs of drifting ice floes and at fixed locations are being added to the archive as they become declassified.

NTM capabilities have been used to provide coincident coverage in support of NASA Operation IceBridge airborne campaigns (www.nasa.gov/mission_pages/icebridge/) and the U.S. Office of Naval Research marginal ice zone research project (www.apl.washington.edu/project/project.php?id=miz). For the latter, NTM images are being used to investigate small-scale fracturing in individual ice floes, floe size distribution, melt pond size and melt extent (e.g., Fig. SB5.3) and ocean surface wave characteristics.

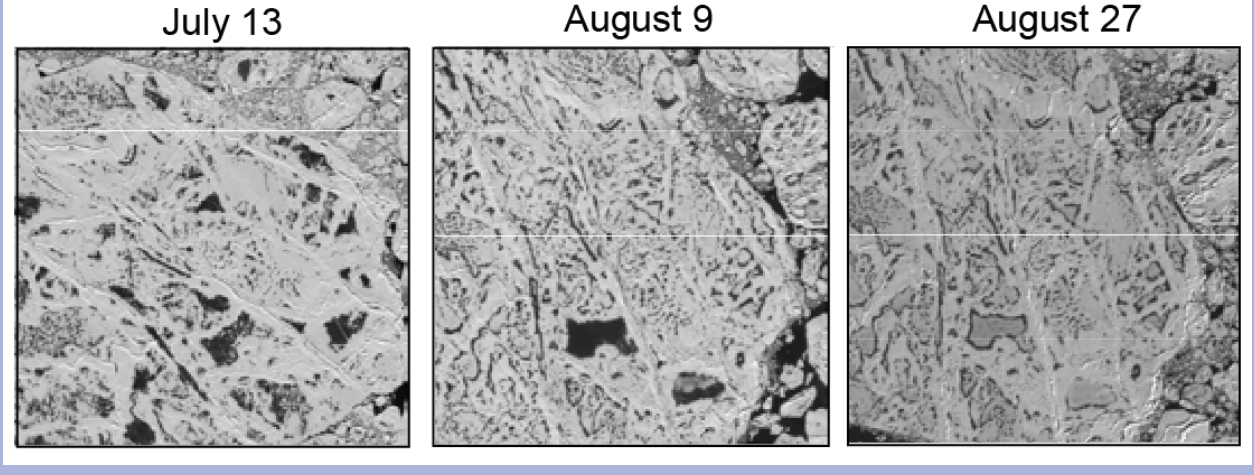

Fig. SB5.3. Melt ponds on the surface of the same drifting ice floe between mid-July and late August. Snow accumulation and surface freezing on August 27 are evident. Each image has dimensions of 1.36 km × 1.36 km and 1-m pixel size.

h. Lake ice—C. R. Duguay, L. C. Brown, K.-K. Kang, and H. Kheyrollah Pour

Lakes with a seasonal ice cover are an important component of the terrestrial landscape. They cover approximately 3.3% of the land area north of 58°N (calculated from the global database of lakes, reservoirs, and wetlands; Lehner and Döll 2004) and, when ice-free, have the highest evaporation rates of any high-latitude terrestrial surface. The duration of lake ice in particular controls the seasonal heat budget of lake systems and thus determines the magnitude and timing of evaporation. The presence (or absence) of ice cover on lakes during the winter months also affects both regional climate and weather events, for example, by thermal moderation and lake-effect snow (Kheyrollah Pour et al. 2012; Zhao et al. 2012).

Lake ice is also a sensitive indicator of climate variability and change. Documented trends and variability in lake ice conditions have largely been related to air temperature changes and, to a lesser extent, snow cover. Long-term trends in ground-based records reveal increasingly later freeze-up (ice-on) and earlier break-up (ice-off) dates, closely corresponding to increasing air temperature trends. Broad spatial patterns in these trends are also related to major atmospheric circulation patterns originating from the Pacific and Atlantic Oceans, for example, the El Niño–La Niña/Southern Oscillation, the Pacific North American pattern, the Pacific decadal oscillation, and the North Atlantic Oscillation/Arctic Oscillation (Bonsal et al. 2006; Prowse et al. 2011).

Notwithstanding the robustness of lake ice as an indicator of climate change, a dramatic reduction in ground-based observations has occurred globally since the 1980s (Duguay et al. 2006; IGOS 2007; Jeffries et al. 2012). Consequently, satellite remote sensing has assumed a greater role in observing lake ice phenology, that is, freeze-up and break-up (Geldsetzer et al. 2010; Brown and Duguay 2012; Kang et al. 2012; Duguay et al. 2015). In figure 5.20, pan-Arctic ice phenology and ice cover duration, derived from the NOAA Interactive Multisensor Snow and Ice Mapping System (IMS; Helfrich et al. 2007) 4-km resolution grid daily product for the 2013/14 ice season, are compared to average conditions of the satellite historical record available since 2004. The IMS incorporates a wide variety of satellite imagery, derived mapped products, and surface observations.

Freeze-up in 2013/14 occurred earlier than the 2004–13 average by ~1–3 weeks for many regions of the Arctic (northern Scandinavia, Alaska and Yukon, Canadian Arctic Archipelago, Great Slave Lake, and Lake Athabasca; Fig. 5.20a). Some exceptions include

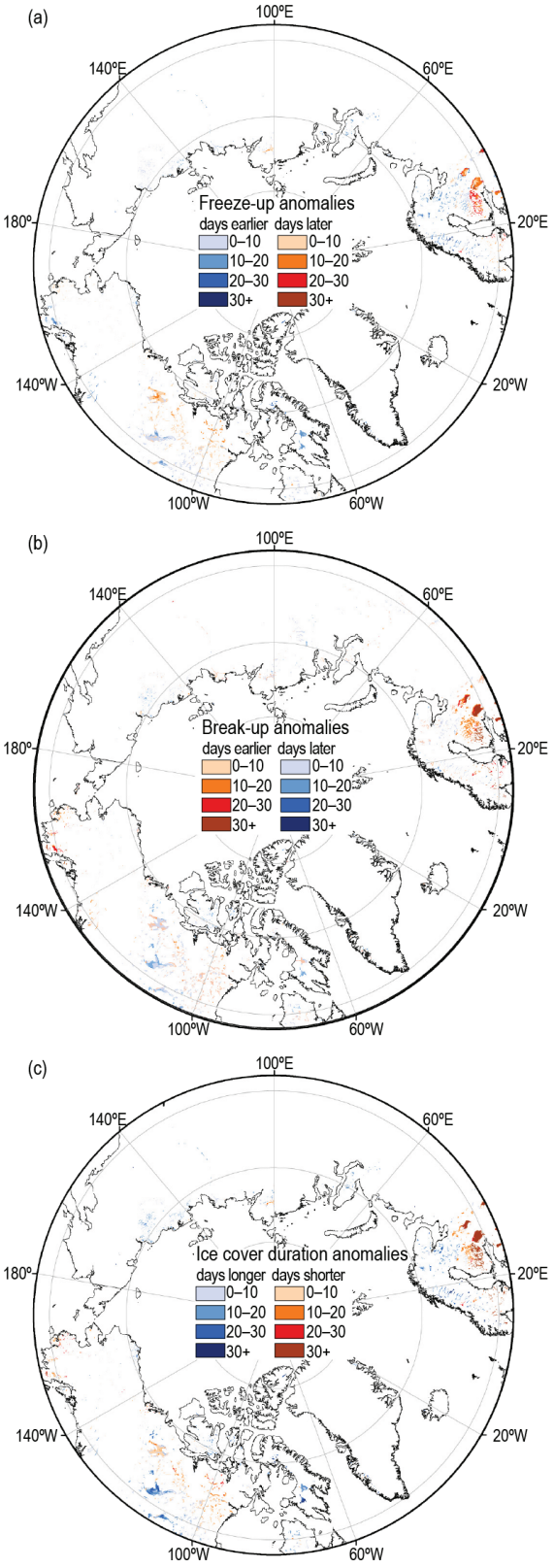

Fig. 5.20. (a) Freeze-up, (b) break-up, and (c) ice cover duration anomalies for the 2013/14 ice season relative to the 2004–13 mean from the NOAA IMS 4-km product. Freeze-up and break-up dates, and ice duration were derived at the pixel level.

lakes in western Russia (Ladoga and Onega), lakes of smaller size in southern Finland and southern Sweden (~2–4 weeks earlier) as well as Great Bear Lake in Canada and smaller lakes at similar latitude to the east (~1–2 weeks later). The earlier freeze-up period of 2013/14 is in sharp contrast to that of 2012/13 for lakes in western Russia and in southern Finland, where freeze-up was ~1–2 months later (Duguay et al. 2014).

Break-up dates in 2014 occurred ~2–6 weeks earlier than the 2004–13 average over much of Scandinavia and western Russia as well as southwestern Alaska and Yukon. Notable exceptions include Great Slave Lake and Lake Athabasca as well as most lakes of the Canadian Arctic Archipelago and eastern Siberia (~1–3 weeks later; Fig. 5.20b). Lakes showing the largest break-up anomalies with earlier dates in 2014 (~3–6 weeks earlier in Scandinavia and western Russia) are consistent with winter- and springtime positive air temperature anomalies and record low April 2014 snow extent (see sections 5b and 5d). Break-up dates are in striking contrast to those of 2013 for these lake regions (Duguay et al. 2014), with break-up occurring ~2 months earlier in 2014.

Ice cover duration (Fig. 5.20c) for 2013/14 was generally shorter by ~2–6 weeks in western Russia, southern Finland and southern Sweden, southwestern Alaska, and Great Bear Lake and lakes to its east (west of Hudson Bay). For some sections of Ladoga and smaller nearby lakes, the ice season was up to 12 weeks shorter compared to the 2004–13 average. Ice cover duration was longer by ~1–4 weeks for lakes of the Canadian Arctic Archipelago, Great Slave Lake and Lake Athabasca, eastern Siberia, and most lakes of Norway as well as northern Sweden and northern Finland. When comparing ice seasons 2013/14 and 2012/13 (Duguay et al. 2014), the largest differences in ice cover duration are observed in Scandinavia and western Russia. In general, ice cover duration was shorter by ~2 months to the south and longer by ~1 month to the north of this region in 2013/14.

i. Sea ice cover—D. Perovich, S. Gerland, S. Hendricks, W. Meier, M. Nicolaus, and M. Tschudi

Three key variables are used to describe the state of the ice cover: ice extent, age of the ice, and ice thickness. Sea ice extent is used as the basic description of the state of the Arctic sea ice cover. Satellite-based passive microwave instruments have been used to estimate sea ice extent since 1979. Two months each year are of particular interest: September, at the end of summer, when the sea ice reaches its annual minimum extent, and March, at the end of winter, when the ice is at its maximum extent (Fig. 5.21).

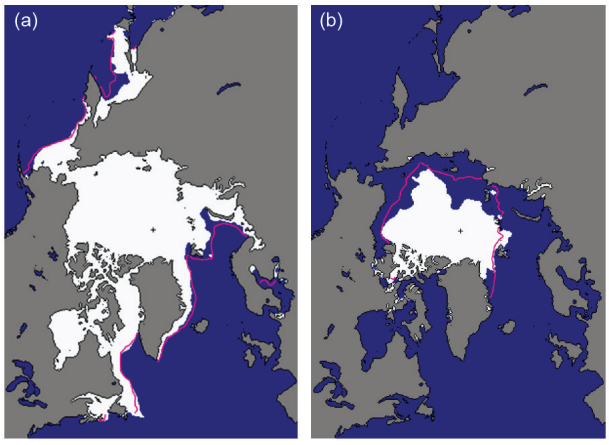

Fig. 5.21. Sea ice extent in (a) Mar 2014 and (b) Sep 2014, illustrating the respective monthly averages for the winter maximum and summer minimum extents. The magenta lines indicate the median ice extents in Mar and Sep, respectively, for the period 1981–2010. (Source: NSIDC, http://nsidc.org/data/seaice_index.)

Based on estimates produced by the National Snow and Ice Data Center (NSIDC) the sea ice cover reached a minimum annual extent of 5.02 million km^2 on 17 September 2014. This was substantially higher (by 1.61 million km^2) than the record minimum of 3.41 million km^2 set in September 2012 but was still 1.12 million km^2 (23%) below the 1981–2010 average minimum ice extent (Fig. 5.21b). The eight lowest sea ice extent minima in the satellite record (1979–2014) have all occurred in the last eight years (2007–14).

In March 2014, ice extent reached a maximum value of 14.76 million km^2 (Fig. 5.21a), 5% below the 1981–2010 average. This was slightly less than the March 2013 value, but was typical of the past decade (2005–14).

The September monthly average trend in sea ice extent is now –13.3% decade^{-1} relative to the 1981–2010 average (Fig. 5.22). The trend is smaller for March (–2.6% decade^{-1}) but is still decreasing at a statistically significant rate. There was a loss of 9.48 million km^2 of ice between the March and September average maximum and minimum extents in 2014. This is the smallest annual seasonal decline since 2006, but still 500 000 km^2 more than the average seasonal loss.

The age of the sea ice serves as an indicator of ice physical properties, particularly thickness. Older ice tends to be thicker and thus more resilient to changes in atmospheric and oceanic forcing compared to younger ice. The age of the ice has been estimated using satellite passive microwave observations and drifting buoy records to track ice parcels over several years (Tschudi et al. 2010; Maslanik et al. 2011). This

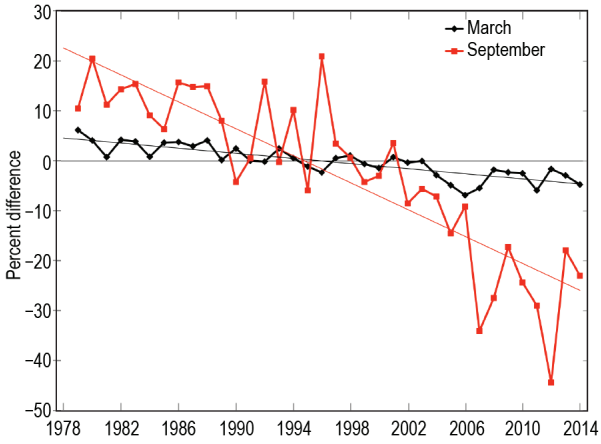

Fig. 5.22. Time series of Arctic sea ice extent anomalies in Mar (black symbols) and Sep (red symbols). The anomaly value for each year is the difference (in %) in ice extent relative to the mean values for 1981–2010. The thin black and red lines are least squares linear regression lines. The slopes of these lines indicate ice losses of –2.6% and –13.3% decade^{-1} in Mar and Sep, respectively, during the period of satellite passive microwave observation, 1979–2014.

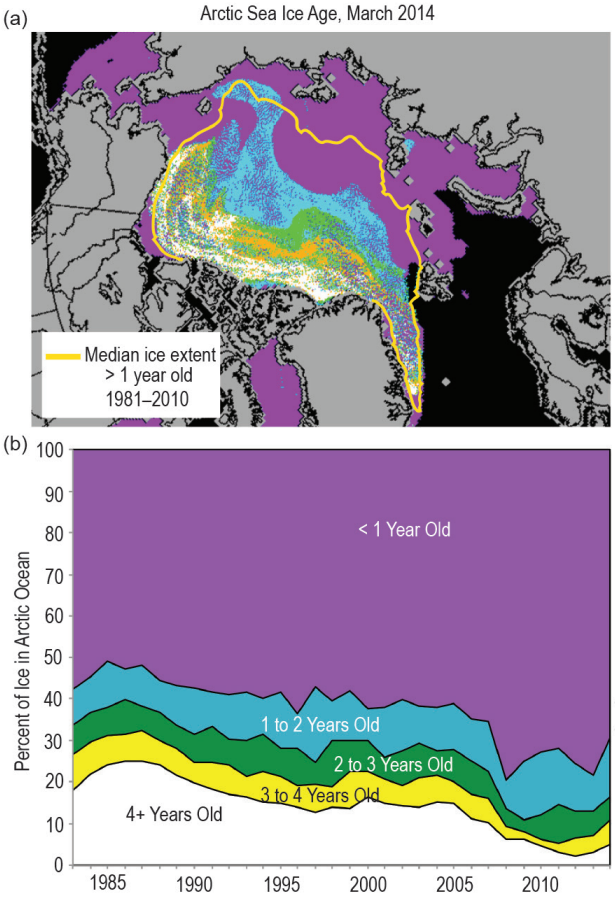

Fig. 5.23. (a) The age of sea ice in March 2014, determined using satellite passive microwave observations and drifting buoy records to track the movement of parcels of ice. The yellow line denotes the median multiyear ice extent for the period 1981–2010. (b) Time series of the percentage of Arctic sea ice in different age categories. The plots are courtesy of J. Maslanik and M. Tschudi (University of Colorado Boulder and the NSIDC).

method has been used to provide a record of ice age since the early 1980s.

The coverage of multiyear ice (any sea ice that has survived at least one melt season) in March 2014 (Fig. 5.23) increased from the previous year. There was a fractional increase in second-year ice (ice that has survived only one melt season), from 8% to 14%, which offset the reduction of first-year ice; it decreased from 78% of the pack in 2013 to 69% in 2014, indicating that a significant proportion of first-year ice survived the 2013 summer melt. The oldest ice (4+ years) fraction (Fig. 5.23b) has also increased, composing 10.1% of the March 2014 ice cover, up from 7.2% the previous year. Despite these changes, there was still much less of the oldest and thickest ice in 2014 than in 1988. In the 1980s the oldest ice made up 26% of the ice pack.

The CryoSat-2 satellite of the European Space Agency has now produced a time series of radar altimetry data for four successive seasons, with sea ice freeboard information (from which ice thickness is derived) available between October and April. The algorithms for deriving freeboard, the height of the ice surface above the water level, and its conversion into sea ice thickness are still being improved (Kurtz et al. 2014; Ricker et al. 2014; Kwok et al. 2014b). Current sea ice thickness data products from CryoSat-2 are based on the assumption that the impact of the snow layer on freeboard is constant from year to year and snow depth can be sufficiently approximated by climatological values. The mean freeboard and thickness values described here were calculated for an area in the central Arctic Ocean where the snow climatology is considered to be valid. Excluded are the ice-covered areas of the southern Barents Sea, Fram Strait, Baffin Bay, and the Canadian Arctic Archipelago.

Using these assumptions, updated freeboard and sea ice thickness maps of the CryoSat-2 data product from the Alfred Wegner Institute Sea Ice Portal (www.meereisportal.de/en) show an increase in average freeboard of 0.05 m in March 2014 compared to the two preceding years (2012: 0.16 m; 2013: 0.16 m; 2014: 0.21 m). This amounts to an increase of mean sea ice thickness of 0.38 m (2012: 1.97 m; 2013: 1.97 m; 2014: 2.35 m). The main increase of mean freeboard and thickness is observed in the multiyear sea ice zone northwest of Greenland, while first-year sea ice freeboard and thickness values (1.5–2 m) remained typical for the Arctic spring.

j. Sea surface temperature—M.-L. Timmermans and A. Proshutinsky

Arctic Ocean sea surface temperature (SST) is an important climate indicator that shows the integrated effect of different factors beyond the seasonal cycle of solar forcing, including heat advection by ocean currents and atmospheric circulation. The distribution of summer SST in the Arctic Ocean largely reflects patterns and timing of sea ice retreat and absorption of solar radiation into the surface layer, which is influenced by cloud cover, water color, and upper ocean stratification. August SSTs are an appropriate representation of Arctic Ocean summer SSTs, avoiding the complications that arise in September when cooling and subsequent sea ice growth typically takes place.

SST data used here are from the NOAA Optimum Interpolation (OI) SST Version 2 monthly product (December 1981–present), a blend of in situ and satellite measurements (Reynolds et al. 2002, 2007). For sea ice concentrations greater than 50%, the NOAA OISST product uses a linear relationship with sea ice concentration to infer SST, with SST constrained to −1.8°C (the freezing point of seawater with a salinity of 33 at the sea surface) where ice cover is 100% (Reynolds et al. 2007). This algorithm does not account for varying seawater freezing temperatures due to varying sea surface salinity. Notable differences in the distribution of near-surface salinities in the Arctic Ocean (see Fig. 5.16 of Timmermans et al. 2014) include fresher surface salinities (~30–31) in the Chukchi Sea compared to the Barents Sea (~34–35); associated variations in freezing temperature imply that SSTs inferred from sea ice can be erroneously cool by as much as 0.2°C, with the highest errors in the Canadian sector.

Mean SSTs in August 2014 in ice-free regions ranged between ~0°C and +7°C, displaying the same general geographic pattern as the August mean for the period 1982–2010 (Fig. 5.24). In August 2014, the warmest SST anomalies were observed in the vicinity of the Bering Strait and the northern region of the Laptev Sea. SSTs in those regions were the warmest since 2007, with values as much as ~4°C warmer than the 1982–2010 August mean (Fig. 5.25d). August 2014 SSTs returned to cooler values in the vicinity of the Barents and Kara Seas (Figs. 5.24a and 5.25d), with close to zero area-averaged SST anomalies compared to the 1982–2010 period (Fig. 5.26a).

In recent summers, many Arctic Ocean marginal seas have had anomalously warm SSTs in August relative to the 1982–2010 August mean (Fig. 5.25). The SST anomaly distribution in August 2007 is notable for the most strongly positive values over large parts

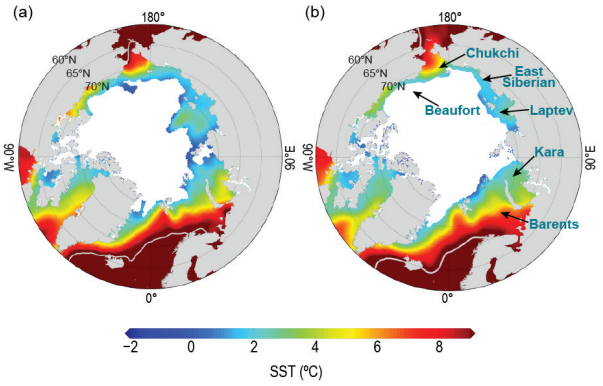

Fig. 5.24. (a) Mean SST (°C) in Aug 2014. White shading is the Aug 2014 mean sea ice extent. (Source: NSIDC) (b) Mean SST in Aug during 1982–2010. White shading indicates the median ice extent in Aug for 1982–2010. Gray contours in both panels indicate the 10°C isotherm.

of the Chukchi, Beaufort, and East Siberian Seas since 1982 (Fig. 5.26a). In August 2007, SST anomalies were up to +5°C in ice-free regions (Fig. 5.25a; Steele et al. 2008); warm SST anomalies of this same order were observed in 2008 (not shown) over a smaller region in the Beaufort Sea (Proshutinsky et al. 2009). Anomalously warm SSTs in those summers were related to the timing of sea ice losses and absorption

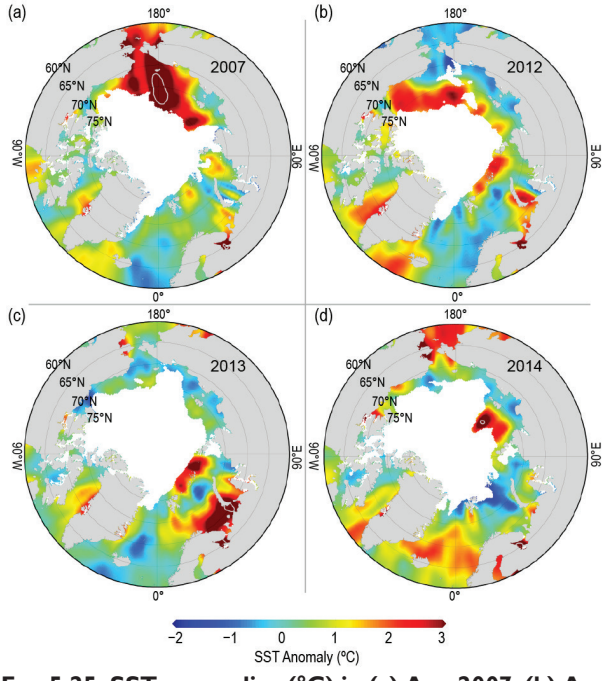

Fig. 5.25. SST anomalies (°C) in (a) Aug 2007, (b) Aug 2012, (c) Aug 2013, and (d) Aug 2014 relative to the Aug mean for the period 1982–2010. White shading in each panel indicates August-average sea ice extent for each year. Gray contours near Iceland in the North Atlantic and in the Bering Strait in the North Pacific indicate the 4°C isotherm.

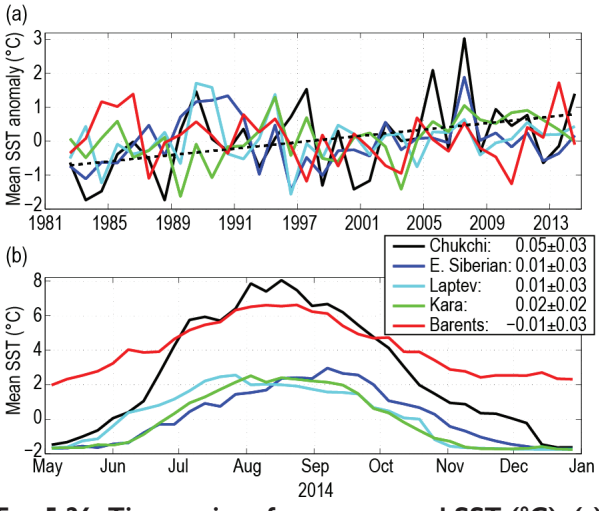

Fig. 5.26. Time series of area-averaged SST (°C): (a) SST anomalies for Aug of each year relative to the Aug mean for the period 1982–2010 for each of the marginal seas (see Fig. 5.24b) of the Arctic Ocean. The dotted black line shows the linear SST trend for the Chukchi Sea (the only marginal sea to show a trend significantly different from zero). Numbers in the legend are the linear trends (with 95% confidence intervals) in °C yr^{-1}. (b) SST from May to Dec 2014 for each of the marginal seas, where the OISST Version 2 weekly product has been used in the calculation.

of incoming solar radiation in open water areas, with ice-albedo feedback playing a principal role (e.g., Perovich et al. 2007). Other regions of anomalously warm SSTs in recent summers include the Barents and Kara Seas, with particularly warm values in August 2013, when the ocean surface was up to 4°C warmer than the 1982–2010 August mean (Fig. 5.25c). SSTs in the southern Barents Sea in summer 2013 reached as high as 11°C; warm waters here can be related to earlier ice retreat in these regions and possibly also to the advection of anomalously warm water from the North Atlantic Ocean (Timmermans et al. 2014).

Cold anomalies have also been observed in some regions in recent summers (Timmermans et al. 2013, 2014). For example, cooler SSTs in the Chukchi and East Siberian Seas in August 2012 and August 2013 were linked to later and less-extensive sea ice retreat in these regions in those years. In addition, a strong cyclonic storm during the first week of August 2012 (Simmonds 2013), which moved eastward across the East Siberian, Chukchi, and Beaufort Seas, caused anomalously cool SSTs as a result of mixing of warm surface waters with cooler deeper waters (Zhang et al. 2013).

Time series of average SST over the Arctic marginal seas, which are regions of predominantly open water in the month of August, are dominated by strong interannual and spatial variability (Fig. 5.26a). The high August SSTs in the Chukchi Sea in 2005 and 2007 are notable features of the record and were due to earlier sea ice reduction in this region relative to preceding years and prolonged exposure of surface waters to direct solar heating. In other marginal seas, warm August SST anomalies observed in recent years are of similar magnitude to warm anomalies observed in past decades. General warming trends are apparent, however, with the most significant linear trend occurring in the Chukchi Sea, where SST is increasing at a rate of about 0.5°C decade^{-1}, primarily as a result of declining trends in summer sea ice extent in the region (e.g., Ogi and Rigor 2013).

The seasonal evolution of SST in the marginal seas exhibited the same general trends and regional differences in 2014 (Fig. 5.26b) as for the preceding decade (not shown). Seasonal warming in the marginal seas begins as early as May and the seasonal cooling period begins as early as mid-August, with cooling observed through December (Fig. 5.26b). Rates of seasonal warming in 2014 were highest in the Chukchi Sea, where mean SSTs increased by ~3°C month^{-1} between mid-May and mid-August. A return to freezing SSTs in the Chukchi Sea occurred more slowly, at a rate of ~−2°C month^{-1} between mid-August and mid-December (Fig. 5.26b). This asymmetry in warming and cooling rates, observed in all years of the 1990–present weekly SST record (not shown), suggests another source of heat in addition to solar radiation; it is likely that advection of warm water from the Bering Sea inhibits SST cooling. Advanced rates of warming (compared to cooling) were also observed in the Barents Sea, which is influenced by warm waters of North Atlantic origin (see Carton et al. 2011), while more symmetric rates of seasonal warming and cooling were observed in the relatively isolated Laptev and East Siberian Seas.